1

Nanoelectrochemistry of Adsorption-Coupled Electron Transfer at Carbon Electrodes

Shigeru Amemiya

Department of Chemistry, University of Pittsburgh, USA

1.1 Introduction

This chapter is concerned with studies of heterogeneous electron transfer (ET) at carbon electrodes when redox-active molecules can be reversibly and specifically adsorbed on the electrode surfaces [1]. These studies of adsorption-coupled ET complement seminal studies of redox-active molecules irreversibly attached to the electrode surfaces [2, 3]. Adsorption-coupled ET is ubiquitous in applied electrochemistry and plays crucial roles in electrocatalysis [4], photocatalysis [4], electrodeposition [5], electropolymerization [6], electrochemical remediation [7], and electroanalysis [8]. For these applications, carbon materials are highly attractive owing to their well-known propensity to adsorb molecules [9, 10]. In fact, significant attention has been given not only to traditional carbon materials, but also to emerging carbon nanomaterials as important electrode materials [11] for diverse applications, especially in energy conversion and storage, e.g. fuel cells [12], batteries [13], solar cells [14], and supercapacitors [15]. This propensity, however, hampers a fundamental understanding of adsorption-coupled ET at carbon electrodes, which are readily contaminated [9, 16, 17]. The adventitious contamination of carbon surfaces has been well recognized [16, 18], but has not been prevented effectively despite a huge body of work on carbon electrochemistry [11, 19]. It has been difficult to reliably characterize the intrinsic electrochemical reactivity and adsorption properties of carbon electrodes [20].

In this chapter, we introduce recent progress in theory of adsorption-coupled ET and its experimental assessment at carbon electrodes. Theoretical progress was made recently by Amatore and coworkers [21, 22], who refined a quantitative model of adsorption-coupled ET developed by Laviron [1, 23] by considering outer- and inner-sphere ET and surface adsorption as elementary electrode steps [24]. Experimental progress were made by the development and nanoelectrochemical characterization of clean carbon electrodes as requisites to reliably examine theories for adsorption-coupled ET. In particular, nanoscale scanning electrochemical microscopy (SECM) [25, 26] serves as an emerging powerful method to quantitatively investigate carbon electrochemistry [27] and beyond.

Nanocarbon Electrochemistry, First Edition. Edited by Nianjun Yang, Guohua Zhao, and John S. Foord.

1.2 Overview of Adsorption-Coupled ET

The specific and reversible adsorption of a redox molecule from the solution to the electrode surface couples heterogeneous outer- and inner-sphere ET as modeled by Laviron [23] and Amatore [24]. In their model (Figure 1.1), a redox molecule, O, is transported from the solution to the outer Helmholtz plane (OHP) [28] near the electrode surface to participate in outer-sphere ET, i.e.

$$O_{sol} + e \rightleftharpoons R_{sol} \tag{1.1}$$

where the transported molecule, O_{sol}, and the product of outer-sphere ET, R_{sol}, can be adsorbed at the inner Helmholtz plane (IHP) [28] of the electrode surface, i.e.

$$O_{sol} \rightleftharpoons O_{ads} \tag{1.2}$$

$$R_{sol} \rightleftharpoons R_{ads} \tag{1.3}$$

When both forms of the redox couple are adsorbed, inner-sphere ET can be mediated, i.e.

$$O_{ads} + e \rightleftharpoons R_{ads} \tag{1.4}$$

In addition, a heterogeneous self-exchange ET reaction is possible as given by

$$O_{ads} + R_{sol} \rightleftharpoons R_{ads} + O_{sol} \tag{1.5}$$

A quantitative understanding of the Laviron–Amatore model requires the knowledge of time-dependent concentrations of four species including O_{ads}, R_{ads}, O_{sol}, and R_{sol} in addition to time- and distance-dependent concentrations of O and R in a diffusion layer near the electrode surface, where the respective concentrations are given by Γ_O, Γ_R, $C_O(0, t)$, $C_R(0, t)$, $C_O(x, t)$, $C_R(x, t)$ (Figure 1.1). Mathematically, adsorption-coupled ET can be modeled by solving two Fickian diffusion equations with four independent equations at the electrode surface as boundary conditions. For instance, the equilibrium adsorption of oxidized and reduced forms of a redox couple is described by two isotherms for competitive adsorption. In addition, two Nernst equations are obtained to describe the equilibrium of outer- and inner-sphere ET. Adsorption isotherms and Nernst equations must be substituted by the corresponding kinetic expressions when equilibrium adsorption or reversible ET is not maintained, respectively.

Historically, the coupling between outer- and inner-sphere ET of a redox couple through specific adsorption and heterogeneous self-exchange ET was proposed by

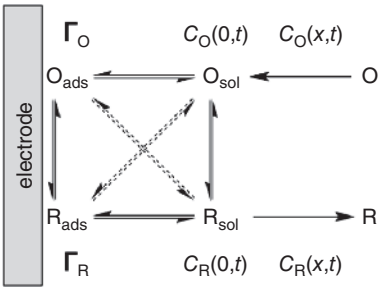

Figure 1.1 The reaction scheme of outer- and inner-sphere ET of non-adsorbed and adsorbed redox molecules, respectively. Dashed arrows indicate heterogeneous self-exchange ET.

Anson in 1961 [29] to account for the anomalous non-linear concentration-dependence of exchange current based on the $Fe^{3+/2+}$ couple at the Pt electrode [30]. Anson's work [29] is theoretically pioneering and insightful, but seems overshadowed by the erroneous assignment of a thin-layer effect to an adsorption effect [29], and is well known rather for the following development of thin-layer electrochemistry [31–33]. Prior to Anson, Laitinen and Randels proposed a model based on inner-sphere ET of tris(ethylenediamine) complexes of Co^{3+} and Co^{2+} adsorbed on the mercury electrode without considering an outer-sphere pathway [34]. Similarly, others also considered only the inner-sphere pathway [35, 36]. Later, Anson attempted to kinetically distinguish between outer- and inner-sphere ET using the Marcus theory [37] and also experimentally identify the electrode reaction mechanism of a redox couple as either outer or inner sphere [38, 39]. More recently, Laviron [23, 40–42] and Amatore [21] theoretically demonstrated conditions where outer- and inner-sphere ET of a redox couple are not distinguishable electrochemically, which will be discussed through this chapter. A redox couple, however, is still considered either as an outer- or inner-sphere couple [4], even controversially [43, 44], despite the possibility that both outer- and inner-sphere pathways can be mediated simultaneously and indistinguishably by the same redox couple.

A quantitative understanding of adsorption-coupled ET is highly challenging even under diffusion-controlled conditions owing to the requirement of adsorption isotherms with multiple parameters. For instance, four parameters are introduced when the adsorption of each form of a redox couple is represented by the simple Langmuir isotherm for competitive adsorption of both forms of the redox couple, to yield [45]

$$\Gamma_O = \frac{\beta_O \Gamma_{O,s} C_O(0,t)}{1 + \beta_O C_O(0,t) + \beta_R C_R(0,t)} \tag{1.6}$$

$$\Gamma_R = \frac{\beta_R \Gamma_{R,s} C_R(0,t)}{1 + \beta_O C_O(0,t) + \beta_R C_R(0,t)} \tag{1.7}$$

where $\Gamma_{i,s}$ is the saturated surface concentration of species i and β_i is a parameter characterizing the magnitude of adsorbate–substrate interaction. In addition, two Nernst equations must be considered to describe diffusion-controlled outer- and inner-sphere ET. A conventional Nernst equation is given for outer-sphere ET by [46]

$$E = E^{0'}_{OS} - \frac{RT}{nF} \ln \frac{C_R(0,t)}{C_O(0,t)} \tag{1.8}$$

where n is the number of transferred electrons and $E^{0'}_{OS}$ is the formal potential of outer-sphere ET. Equation (1.8) can be combined with Langmuir isotherms, Eqs. (1.6) and (1.7), to yield a Nernst equation for inner-sphere ET as [47]

$$E = E^{0'}_{IS} - \frac{RT}{nF} \ln \frac{\Gamma_R}{\Gamma_O} \tag{1.9}$$

with

$$E^{0'}_{IS} = E^{0'}_{OS} - \frac{RT}{nF} \ln \frac{\Gamma_{O,s} \beta_O}{\Gamma_{R,s} \beta_R} \tag{1.10}$$

Equation (1.10) indicates that the equilibrium of inner-sphere ET is controlled by the equilibrium of outer-sphere ET and surface adsorption, thereby introducing no additional parameter. It should be noted that a formal potential is defined for non-adsorbed redox couples in the electrochemistry literature [48] to represent outer-sphere ET, i.e. $E^{0'}_{OS}$. By contrast, interactions between redox molecules and electrodes were considered in a recent theoretical study to calculate formal potentials [49], which should be more directly relevant to inner-sphere ET, i.e. $E^{0'}_{IS}$, rather than outer-sphere ET.

A comparison of Nernst equations for outer- and inner-sphere ET predicts that these two pathways are thermodynamically coupled or decoupled depending on the adsorptivities of a redox couple. Specifically, outer- and inner-sphere ET are coupled and driven simultaneously when both forms of a redox couple are adsorbed similarly, i.e. $\Gamma_{O,s}\beta_O = \Gamma_{R,s}\beta_R$, to yield $E^{0'}_{IS} = E^{0'}_{OS} = E^{0'}$ in Eq. (1.10). In this case, reduction (or oxidation) is driven through both outer- and inner-sphere pathways simultaneously at $E < E^{0'}$ (or $E > E^{0'}$), thereby yielding an electrochemical response based on the convolution of both pathways. By contrast, outer- and inner-sphere ET are decoupled when O (or R) is adsorbed more strongly than the other, i.e. $\Gamma_{O,s}\beta_O >> \Gamma_{R,s}\beta_R$ (or $\Gamma_{O,s}\beta_O << \Gamma_{R,s}\beta_R$), to yield $E^{0'}_{IS} << E^{0'}_{OS}$ (or $E^{0'}_{IS} >> E^{0'}_{OS}$). Specifically, the stronger adsorption of a reactant, O (or R), thermodynamically hampers inner-sphere reduction (or oxidation), which requires more negative (or positive) potentials than required for the outer-sphere counterpart. By contrast, inner-sphere ET is thermodynamically facilitated to require less extreme potentials when a product is more strongly adsorbed on the electrode surface. This thermodynamic assessment reveals a misconception in a recent study that the adsorption of hard-to-reduce metal ions, e.g. Ca^{2+}, on the electrode surface facilitates their inner-sphere reduction to yield voltammetric responses within the potential window [50].

1.3 Clean Carbon Electrodes

Experimentally, a clean carbon surface is required to reliably study adsorption-coupled ET, because both heterogeneous ET [51–54] and surface adsorption [55] can be affected by adventitious surface contamination. Historically, methods have been well established to obtain, maintain, and ensure clean surfaces of metal electrodes, especially Pt [56]. A flame-annealing method was pioneered by Clavilier [57] and is widely used to reproducibly yield clean surfaces of single-crystal metal electrodes. This method, however, is not applicable to carbon materials, which are cleaned by solvents, laser illumination, (vacuum) heat treatment, electrochemical polarization, mechanical polishing, plasma treatment, and chemical oxidation [58]. These methods, however, can be destructive for graphitic materials, especially nanomaterials [58]. Moreover, a flame-annealed metal electrode must be immediately immersed in ultrapure water to prevent airborne contamination, which quickly occurs also on carbon surfaces [17, 59–61]. The ultrapure water must be free from organic, surface-active impurities, which was originally achieved by pyrocatalytic distillation [62] to lower a total organic carbon (TOC) to 3 ppb [63]. Currently, ultrapure water with TOC at the level of 1 ppb is obtainable by UV photooxidation of organic contaminants [64] using commercial water purifiers [65]. Finally, the in-situ cleanliness of a Pt surface in an electrolyte solution can be quantitatively evaluated by studying the electrosorption of hydrogen

[56]. There is, however, no established method to validate the in-situ cleanliness of a carbon electrode surface in an electrolyte solution.

Recent studies showed that the prevention of adventitious organic contamination on the surface of a carbon electrode is still highly challenging. The surface of highly oriented pyrolytic graphite (HOPG) and graphene is quickly contaminated by airborne hydrocarbons, as confirmed by water contact angle (WCA) measurement, attenuated total internal reflectance Fourier transform infrared spectroscopy (ATR-FTIR), and ellipsometry [17, 60]. The heterogeneous distribution of disordered adsorbates on the graphene surface was also observed by atomic force microscopy (AFM) [66]. Traditionally, a freshly exposed HOPG surface was electrochemically characterized as quickly as possible to minimize airborne contamination [67–69]. These studies, however, reported very different ET kinetics [20, 68]. Moreover, the contamination of a freshly HOPG surface in water was revealed by SECM–AFM [70, 71], but not by scanning electrochemical cell microscopy (SECCM) [68, 72], where the surface of a target substrate was always exposed to ambient air.

Recently, we demonstrated that the clean surfaces of sp^2 carbons, i.e. HOPG and graphene, can be protected from airborne contamination simply by condensing a nanometer-thick adlayer of water on the surfaces in humidified air [61] (Figure 1.2a). The WCA of an unprotected HOPG surface quickly increased from ~60° to ~90° in ambient air at room temperature until the surface was saturated with hydrophobic contaminants (Figure 1.2b [61]) as detected by ATR-FTIR. By contrast, the WCA of a HOPG surface increased only to ~70° in ~20 minutes when exfoliated and stored in humidified air at −20 °C to condense a water adlayer, thereby estimating the maximum surface coverage of ~33% with airborne contaminants. The water-protected HOPG surface showed no damage, as confirmed by X-ray photoelectron spectroscopy (XPS). Moreover, ATR-FTIR of the protected HOPG surface showed OH bond stretching at a lower frequency, which indicates the formation of an ice-like structure. The quantitative analysis of ellipsometry data indicated the formation of submonolayer water with a thickness of 0.08 nm on the HOPG surface.

More recently, we developed a new method to protect the pristine surface of electron-beam-deposited carbon (eC) by using a KCl layer (Figure 1.3). The amorphous eC film consists of a mixture of sp^2 and sp^3 hybridized carbon [74] in contrast to HOPG and graphene. The thin eC film was deposited on a metal support to yield sufficient conductivity for electrochemistry as well as molecular electronics [75–78]. Earlier studies showed that the low background current and sufficient transparency of the thin eC film are advantageous for conventional electrochemistry [74] and optical spectroscopy [79, 80], respectively. Technically, we deposited all layers of electrode materials including a KCl layer in vacuum to obtain the pristine eC surface, which was exposed for the first time when the protective KCl layer was dissolved in the aqueous electrolyte solution of redox molecules. The exposed eC surface was extremely flat, as represented by average and root-mean-square roughness of 0.34 ± 0.01 and 0.43 ± 0.02 nm, respectively, based on AFM measurements. Raman and X-ray photoelectron spectroscopies were employed [76] to determine an approximately 70 : 30 ratio of sp^2 and sp^3 hybridized carbon. Advantageously, KCl-protected electrodes are storable and transportable in ambient air without compromising surface cleanliness. In fact, KCl-coated eC samples were prepared in Edmonton and exposed to ambient air during shipment to Pittsburgh to maintain the cleanliness of the underlying eC surface

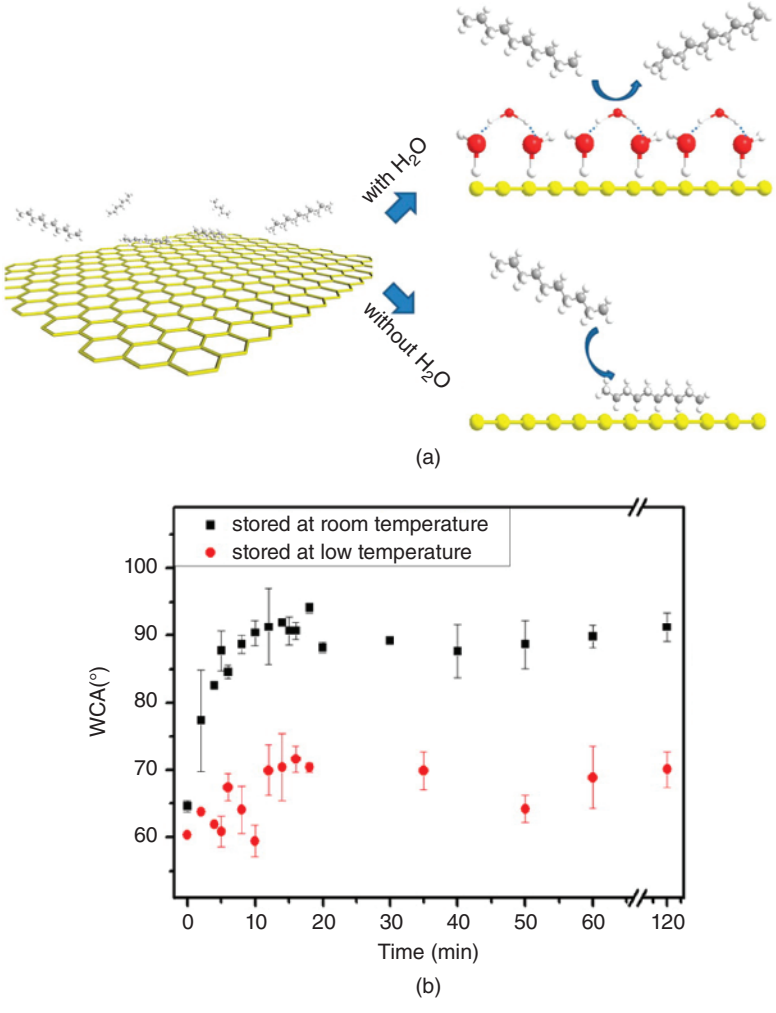

Figure 1.2 (a) Scheme of graphite surface protected from airborne hydrocarbon contaminants by a water adlayer. Yellow, red, white, and gray balls represent sp^2 carbon, oxygen, hydrogen, and sp^3 carbon atoms. (b) Temporal evolution of the WCA measured on freshly exfoliated HOPG stored at room temperature and low temperature. For the sample stored at low temperature, it was only exposed to room temperature during the WCA measurement. Source: Reprinted with permission from Li et al. [61]. Copyright 2016 American Chemical Society.

as ensured by SECM-based nanogap voltammetry (NV) (see below). Potentially, the KCl-based protection method will be applicable to a variety of clean electrode materials prepared in vacuum.

The cleanliness of a macroscopic electrode is maintainable in ultrapure water with low TOC of 2–3 ppb containing high-purity inorganic electrolytes, because of slow linear diffusion of organic impurities to the large electrode surface, as predicted theoretically and confirmed experimentally using HOPG in our recent work [51]. Specifically, we applied a model based on the diffusion-limited and irreversible adsorption of organic

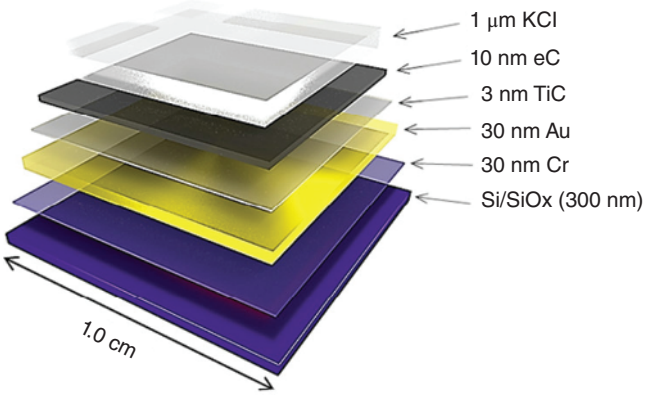

Figure 1.3 Schematic illustration of deposited layers with indicated thicknesses on Si/SiOx substrate. Source: Reprinted with permission from Morteza Najarian et al. [73]. Copyright 2017 American Chemical Society.

impurities [65] to a planar macroscopic surface to estimate the surface coverage of contaminants, θ_c, as given by [51]

$$\theta_c = \frac{2c_c}{\theta_{sat}\rho_c}\sqrt{\frac{D_c t}{\pi}} \tag{1.11}$$

where c_c and D_c are the concentration and diffusion coefficient of organic impurities, respectively, t is the duration of contamination, θ_{sat} is a saturation coverage of the HOPG surface (= 0.14 for benzene [81] as a model for the sake of generality [65]), and ρ_c is the density of carbon atom at the graphite surface ($= 6.3 \times 10^{-9}$ mol cm^{-2}). Equation (1.11) predicts that ultrapure water with TOC values of 2–3 ppb (e.g. 28–42 nM benzene) gives extremely low θ values of 0.0066–0.0099 with $t = 1$ hour. A substantial θ value of 0.066, however, is expected from Eq. (1.11) with $t = 1$ hour when the HOPG surface is immersed in ultrapure water with a TOC value of 20 ppb ($c_c = 0.28$ μM for benzene), which is typically obtained using only filters to remove organic impurities [63]. By contrast, the original model was developed to predict that nanoelectrodes are quickly contaminated even in ultrapure water with a TOC value of 1 ppb owing to fast mass transport of organic impurities to compromise the electroactivity of nanoelectrodes [65], e.g. oxygen reduction at Pt nanoelectrodes [82].

1.4 SECM-Based Nanogap Voltammetry

In-situ cleanliness of a carbon electrode surface was checked experimentally by NV based on SECM. Originally, SECM-based NV was developed to reliably measure fast kinetics of nearly reversible ET by monitoring both oxidation and reduction of a redox couple at quasi-steady states under high mass-transport conditions across a nanometer-wide gap between an ultramicroelectrode (UME) tip and a macroscopic substrate electrode [83]. When an only reduced form of a redox couple, R, is initially present in the solution, the SECM feedback mode is employed to investigate the reduction of the redox couple on the substrate (e.g. eC in Figure 1.4a). Specifically, the

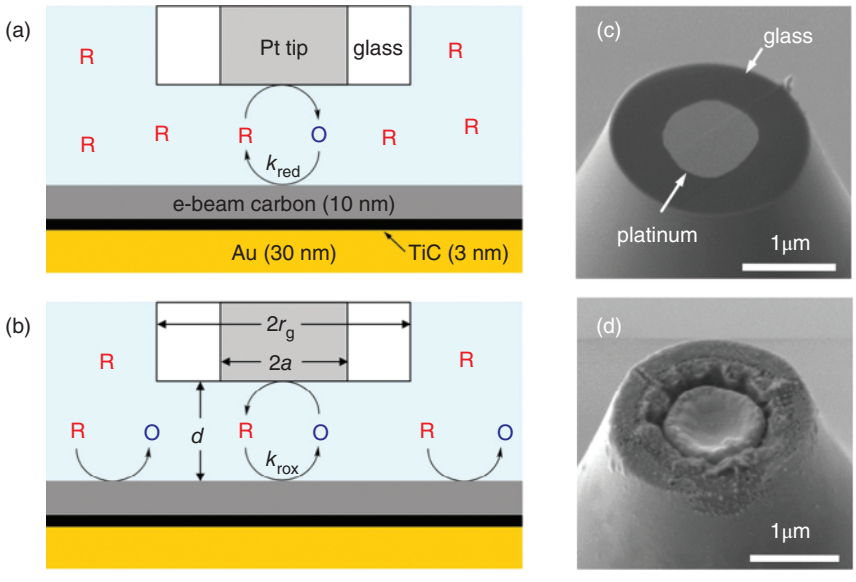

Figure 1.4 Scheme of (a) feedback and (b) SG/TC modes of SECM for NV at an eC electrode. Heterogeneous reduction and oxidation rate constants are represented by k_{red} and k_{ox}, respectively. Source: Reprinted with permission from Morteza Najarian et al. [73]. Copyright 2017 American Chemical Society. SEM images of a borosilicate-sealed Pt UME (c) before and (d) after electrowstatic damage. Source: Reprinted with permission from Nioradze et al. [84]. Copyright 2013 American Chemical Society.

diffusion-limited oxidation of the reductant at the SECM tip yields an amperometric tip current, which varies with the substrate potential. The tip current is enhanced at sufficiently negative potentials, where the reductant is regenerated from the tip-generated oxidant, O, to complete efficient redox cycling across a narrow gap between the tip and the substrate. This positive feedback effect is reduced to eventually diminish the tip current at positive potentials, where the reductant is oxidatively consumed at the substrate, i.e. a shielding effect [85]. By contrast, the oxidation of the reductant at the substrate surface is monitored in the substrate generation/tip collection (SG/TC) mode by detecting the substrate-generated species, O, at the tip (Figure 1.4b). Overall, a pair of NVs is obtained by plotting the amperometric tip current against the substrate potential in feedback and SG/TC modes. The resultant voltammograms are obtained under quasi-steady states to yield a sigmoidal shape when the tip–substrate distance is sufficiently narrow. The NV approach based on complementary operation modes is more reliable than the measurement of single steady-state voltammograms based on either oxidation or reduction of a redox couple, as originally demonstrated for ion-transfer nanopipet voltammetry [86, 87]. It should be noted that SECM-based NV enabled the determination of high k^0 values of up to 25 cm s^{-1} [52] by scanning the potential of a macroscopic substrate around the formal potential of a redox couple under quasi-steady-state conditions [83]. By contrast, macroscopic substrates have been studied by the feedback mode of SECM to predict measurable ET rate constants of up to 20 cm s^{-1} [88], which were recently misrepresented as measurable k^0 values [89], i.e., ET rate constants at the formal potential. The measurable ET rate constants

correspond to lower k^0 values of up to ~2 cm s^{-1} even with nanogap configurations [90], because the substrate potential is usually far from the formal potential in the feedback mode of SECM to irreversibly electrolyze the tip-generated species at the substrate, which is required to achieve steady states.

Technologically, the development of SECM-based NV revealed and overcame challenges that were unrecognized previously [25]. The formation of a nanogap requires a flat region of a substrate under a small tip with well-defined flat geometry (Figure 1.4c), which was found compromised by electrostatic damage from an experimenter (Figure 1.4d) and a (bi-)potentiostat [84, 91, 92]. Moreover, it was found that the maintenance of a nanogap with a fixed width required the elimination of the nanoscale thermal drift of tip position [92, 93]. The importance of preventing tip damage and thermal drift was overlooked in earlier studies [94, 95], where only the feedback mode was employed in SECM-based NV of tip reactions to obtain unreliable ET kinetics as revealed in a recent study [96]. It should be emphasized that the finding of electrostatic damage of submicrometer- and nanometer-sized electrodes is new and significant, because the possibility of ill-defined geometry of nanometer-sized electrodes had been pointed out, but attributed to imperfect electrode fabrication [97–100] rather than the damage of well-fabricated electrodes. Moreover, the damage of nanoelectrodes was unseen previously [101, 102], but was noticed [103] after the problem was reported [84].

SECM-based NV was used to ensure the cleanliness of KCl-protected eC surface [73]. Both SG/TC and feedback modes of SECM were employed to investigate the oxidation and reduction of the FcTMA$^{2+/+}$ couple, respectively, at KCl-protected and non-protected eC electrodes (Figure 1.5a,b, respectively). When the eC surface was protected by a KCl layer, symmetric pairs of reversible NVs were obtained at tip–substrate distances of down to 49 nm. The shortest tip–substrate distance was used to estimate

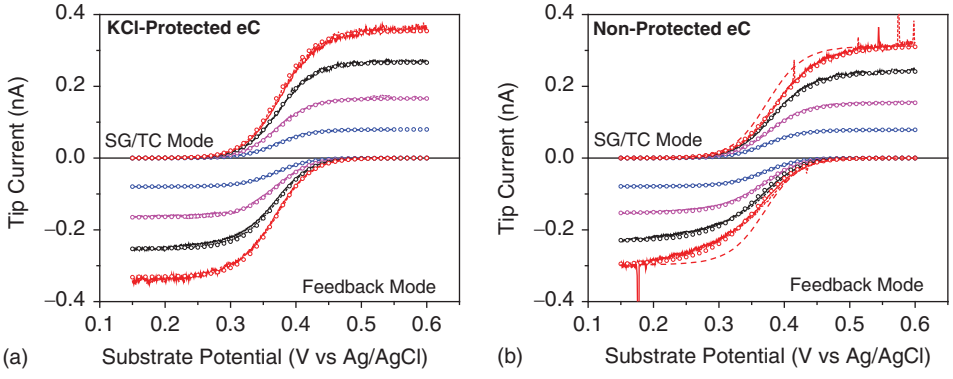

Figure 1.5 Nanogap voltammograms of 0.3 mM FcTMA$^+$ in 1 M KCl at eC electrodes prepared without (a) and with (b) a protective KCl layer obtained using 1.01 and 1.04 µm-diameter Pt tips, respectively. Forward and reverse waves are represented by solid and dotted lines, respectively. Tip potentials, 0.55 and 0.15 V vs Ag/AgCl in feedback and SG/TC modes, respectively. Potential sweep rate, 0.05 V s^{-1}. Circles represent theoretical curves with $E^{0'}$ = 0.371 V vs Ag/AgCl and gap widths of 44–275 nm. Dashed lines in panel B represent theoretical reversible curves at the shortest tip—substrate distance of 49 nm. Source: Reprinted with permission from Morteza Najarian et al. [73]. Copyright 2017 American Chemical Society.

the diffusion-limited minimum k^0 value of 14 cm s^{-1}, which is equivalent to $k^0a/D = 10$ with a tip radius, a, of 0.52 μm and a diffusion coefficient, D, of 6.0×10^6 cm^2 s^{-1}. The minimum k^0 value is one of the highest k^0 values estimated for a ferrocene derivative at carbon and metal electrodes (Table 1.1) as discussed further below. By contrast, NVs at non-protected eC surfaces were kinetically limited to yield a finite k^0 value of 1.45 cm s^{-1}, which is at least 10 times lower than the k^0 value at the KCl-protected eC surface. Importantly, the high k^0 value at the clean eC surface is attributed to a standard rate constant of outer-sphere ET, k^0_{OS}, because the eC surface adsorbs $FcTMA^+$, but not $FcTMA^{2+}$, i.e. $\Gamma_{R,s}\beta_R >> \Gamma_{O,s}\beta_O$, to thermodynamically decouple inner-sphere oxidation of adsorbed $FcTMA^+$ to much more positive potentials. The minimum k^0_{OS} value of 14 cm s^{-1} is still lower than a k^0_{OS} value of 100 cm s^{-1} predicted for the $FcTMA^{2+/+}$ couple [104] by Marcus theory [108]

$$k^0_{OS} = Z_{het}(k_{ex}/Z_{bi})^{1/2} \tag{1.12}$$

where k_{ex} is a homogeneous self-exchange rate constant, and Z_{het} ($\sim 10^4$ cm s^{-1}) and Z_{bi} ($\sim 10^{11}$ M^{-1} sec^{-1}) are heterogeneous and bimolecular collision frequencies, respectively. Equation (1.12) assumes adiabatic conditions, where outer-sphere ET is controlled by the reorganization of the redox couple and surrounding solvents to yield the highest possible k^0_{OS} value. The adiabatic k^0_{OS} value of 100 cm s^{-1} for $FcTMA^+$ is nearly identical to the highest k^0 value that can be measured by SECM, which is limited by electron tunneling across a narrow gap between the tip and the substrate [109].

We employed SECM-based NV also to study a clean surface of HOPG [104], which was protected by a nanometer-thick water adlayer condensed on the HOPG surface freshly peeled in humidified air [61]. The in-situ cleanliness of water-protected HOPG was ensured by a symmetric pair of NVs for the $FcTMA^{2+/+}$ couple in feedback and

Table 1.1 Standard ET rate constants of $FcTMA^+$ and $FcCH_2OH$ at carbons and Pt.

Electrode	Ferrocene	k^0 (cm s^{-1})	Method	Ref.
—	$FcTMA^+$	100[a)]	—	[104]
eC (KCl protection)	$FcTMA^+$	≥14	SECM[b)]	[73]
eC	$FcTMA^+$	1.45 ± 0.06	SECM[b)]	[73]
HOPG (water protection)	$FcTMA^+$	≥12	SECM[b)]	[104]
HOPG	$FcTMA^+$	≥17, ≥13	SECM[b)]	[51]
HOPG	$FcTMA^+$	1.7 ± 0.3, 0.7 ± 0.3	SECM	[51]
HOPG	$FcTMA^+$	≥0.1–1.0	SECCM[c)]	[105]
SWCNT	$FcTMA^+$	9 ± 2	SECCM[c)]	[106]
SWCNT (metallic)	$FcTMA^+$	7 ± 2	SECCM[c)]	[107]
SWCNT (semi-conductive)	$FcTMA^+$	4 ± 2	SECCM[c)]	[107]
Pt nanoelectrode	$FcCH_2OH$	>20	SECM[b)]	[96]
	$FcCH_2OH$	6.8 ± 0.7	SECM	[94]

a) Marcus theory (Eq. (1.12)).
b) low-TOC water.
c) ambient air.

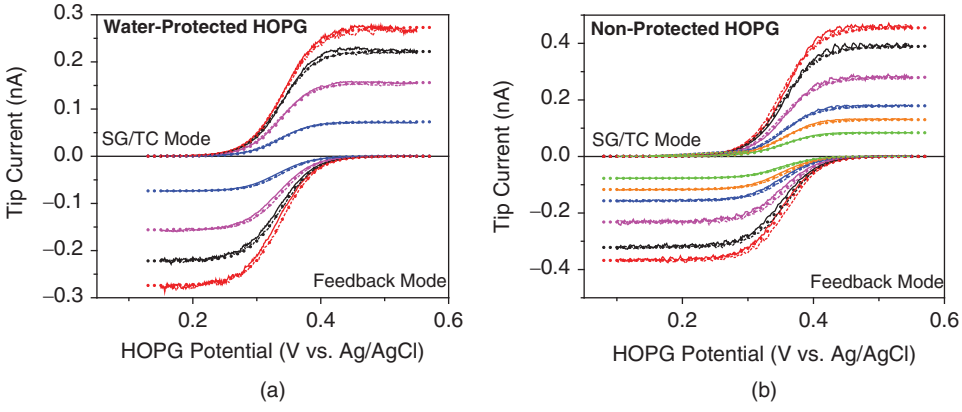

Figure 1.6 (a) Symmetric and (b) asymmetric pairs of nanogap voltammograms of 0.3 mM $FcTMA^+$ at water-protected and non-unprotected HOPG surfaces, respectively, as obtained using 1.0 µm-diameter Pt tips in 50 mM KCl. Forward and reverse waves are represented by solid and dashed lines, respectively. Dots represent reversible voltammograms without any adsorption effect simulated with $E^{0'} = 0.340$ V and gap widths of (a) 52–270 nm and (b) 45–309 and 36–271 nm in feedback and SG/TC modes, respectively. Tip potentials, 0.5 and 0.15 V vs Ag/AgCl in the respective modes. Potential sweep rate, 0.05 V s^{-1}. Source: Reprinted with permission from (a) Nioradze et al. [51] (Copyright 2015 American Chemical Society) and (b) Chen et al. [104] (Copyright 2016 American Chemical Society).

SG/TC modes (Figure 1.6a). This result also confirmed that the anomalous asymmetry of a pair of NVs for the $FcTMA^{2+/+}$ couple at non-protected HOPG (Figure 1.6b) was due to airborne contamination [51]. More quantitatively, symmetric pairs of NVs at water-protected HOPG were reversible to yield diffusion-limited minimum k^0 values of up to 12 cm s^{-1} consistently in both feedback and SG/TC modes at the shortest tip–substrate distance of 55 nm. Asymmetric pairs of NVs at non-protected HOPG were also reversible, but inconsistent in their heights to yield different minimum k^0 values of 17 and 13 cm s^{-1} in SG/TC and feedback modes, respectively. The lower limiting current in the feedback mode was attributed to the lower permeability of a hydrophobic contaminant layer to $FcTMA^{2+}$, which is reduced at the underlying HOPG surface in the feedback mode. By contrast, the contaminant layer is more permeable to more hydrophobic $FcTMA^+$, which is oxidized in the SG/TC mode to yield a higher limiting current and, subsequently, an apparently larger k^0 value. It should be noted that the asymmetry of NVs was misattributed to surface adsorption and self-exchange reactions of the $FcTMA^{2+/+}$ couple by others [110]. We demonstrated that the adsorption of $FcTMA^+$ on HOPG was seen as hysteresis of each NV during the potential cycle (Figure 1.6), but was too weak to simulate the asymmetry of NVs between feedback and SG/TC modes [104]. Moreover, we found [111] that incorrect parameters for the adsorption of $FcTMA^+$ on HOPG were determined in the previous studies [55, 110] and inappropriately used to argue very small effects of surface adsorption on SECM-based NV [89, 110]. We also proved that a heterogeneous self-exchange reaction was not relevant, because only $FcTMA^+$ or $FcTMA^{2+}$ was adsorbed on HOPG or the glass sheath of an SECM tip, respectively [112]. Accordingly, the minimum k^0 values were determined for outer-sphere ET of the $FcTMA^{2+/+}$ couple at the HOPG surface, which adsorbs only $FcTMA^+$ to prevent inner-sphere and self-exchange ET [104, 112].

The SECM-based NV study of clean eC and HOPG surfaces revealed the importance of surface cleanliness in kinetic measurements, where contamination not only from the air but also from water should be prevented. The latter effect was manifested by lower k^0 values of 1.7 and 0.7 cm s^{-1} determined for the $FcTMA^{2+/+}$ couple from asymmetric pairs of SECM-based NVs when HOPG was immersed in standard ultrapure water purified only by filters (Table 1.1). More recently it was reported that the k^0 value of $FcCH_2OH$ at Pt nanoelectrodes was much lower in standard ultrapure water (6.8 cm s^{-1} [94]) than in low TOC water (>20 cm s^{-1} [96]) (Table 1.1). The k^0 values measured for $FcTMA^+$ and $FcCH_2OH$ at HOPG and Pt in low-TOC water are higher than k^0 values of <10 cm s^{-1} measured for $FcTMA^+$ at single-wall carbon nanotubes (SWCNTs) [106, 107] and HOPG [105] by using SECCM. Problematically, SECCM measurements expose a substrate surface to ambient air without any prevention of adventitious airborne contamination of not only the substrate surface, but also a submicrometer-sized water droplet formed at the tip of a nanopipet. The TOC of the water droplet was not reported, but is likely compromised by airborne contamination. Such contaminations may be a reason why lower k^0 values of 7 cm s^{-1} were obtained for $FcTMA^+$ even with metallic SWCNTs by SECCM [107]. It should be noted that low k^0 values measured by SECCM at HOPG [105] are diffusion-limited minimum values [89], which manifests that slow mass transport in tapered pipets [113, 114] lowers measurable k^0 values for SECCM in comparison with SECM under high mass-transport conditions across tip–substrate nanogaps.

It should be emphasized that diffusion-limited minimum k^0 values are informative, but are inaccurate. For instance, diffusion-limited minimum k^0 values of 0.1–1.0 cm s^{-1} for $FcTMA^+$ at HOPG were determined by SECCM to imply the possibility that a true k^0 value can be 0.1–12 cm s^{-1} or higher. The former possibility, however, was excluded by our recent study, which yielded a minimum k^0 value of 12 cm s^{-1} at clean HOPG surfaces by using SECM-based NV [104]. This higher minimum value is still lower than predicted for adiabatic outer-sphere ET of $FcTMA^+$ (k^0_{OS} = 100 cm s^{-1}) by Marcus theory and will be likely exceeded in a future SECM study by using a narrower gap. Nanoscale SECM will be useful also to more accurately assess the fast ET kinetics of various redox couples at HOPG, where even lower k^0 values of ~0.5 cm s^{-1} were estimated as diffusion-limited minimum values from reversible cyclic voltammetry (CVs) [69].

SECM-based NV was also employed [52] to reveal that the electrochemical reactivity of cleaner monolayer graphene was much higher than that of contaminated monolayer graphene reported previously (Table 1.2). In previous studies [115–118], graphene electrodes were prepared by a polymer-mediated transfer method [119], where graphene was grown on a metal film (Ni or Cu) by chemical vapor deposition (CVD) and coated with a polymer film, e.g. poly(methyl methacrylate) (PMMA), to etch away the supporting metal film and transfer polymer-coated graphene on a solid support. Problematically, the removal of the polymer film yielded the graphene surface that was damaged and also contaminated with polymer residues [115], which were difficult to remove without further damage [120]. Graphene electrodes prepared by this method yielded consistently low k^0 values of 0.01–0.037 cm s^{-1} for $FcCH_2OH$ as measured by CV [115] and SECM [116, 117] as well as 0.03–0.2 cm s^{-1} for $FcTMA^+$ by SECCM [118]. By contrast, much higher k^0 values of 1.6 cm s^{-1} were obtained for $FcCH_2OH$ at the graphene surface that was freshly exposed by etching the copper film just before SECM-based NV,

Table 1.2 Standard ET rate constants of $FcTMA^+$ and $FcCH_2OH$ at monolayer graphene.

Electrode	Ferrocene	k^0 (cm s^{-1})	Method	Ref.
CVD graphene[a)]	$FcCH_2OH$	0.037	CV	[115]
CVD graphene[a)]	$FcCH_2OH$	0.020 ± 0.004	SECM	[116]
CVD graphene[a)]	$FcCH_2OH$	0.010 ± 0.002	SECM	[117]
CVD graphene[b)]	$FcCH_2OH$	1.6 ± 0.5, 0.5 ± 0.2	SECM[c)]	[52]
CVD graphene[d)]	$FcCH_2OH$	≥25	SECM[c)]	[52]
CVD graphene[a)]	$FcTMA^+$	0.03–0.2	SECCM[e)]	[118]
exfoliated graphene	$FcCH_2OH$	≥0.5	CV	[115]

a) PMMA-mediated transfer.
b) PMMA-supported.
c) low-TOC water.
d) PS-supported.
e) ambient air.

where a PMMA film served only as a support [52]. These higher k^0 values were consistent with diffusion-limited minimum values determined by CV of $FcCH_2OH$ at graphene exfoliated from HOPG [115]. Interestingly, even higher k^0 values of up to 25 cm s^{-1} were determined for the oxidation of $FcCH_2OH$ at graphene supported by a non-polar polystyrene (PS) film. This result suggests the electrochemical transparency of graphene [52], i.e. the electrochemical reactivity of graphene was affected by the underlying polymer film owing to the atomic thickness of graphene. Electrochemical transparency can be important to understand the electrochemical reactivity of multilayer graphene (eventually equivalent to HOPG), which was studied by SECCM to observe an increase in k^0 values with an increase in the number of graphene layers [118]. None of previous studies, however, measured the electrochemical reactivity of unambiguously pristine graphene, which was exposed to ambient air during SECCM measurements [118] and also during electrode fabrication for CV and SECM as demonstrated by asymmetric pairs of NVs [52], thereby requiring the protection of graphene from airborne contamination, e.g. by the water-based protection method [61]. In addition, CVD-grown graphene must be protected from contamination with silicon oxide nanoparticles deposited from quartz furnaces [121, 122].

1.5 Adsorption-Coupled Outer-Sphere ET

Heterogeneous ET must be mediated through an outer-sphere pathway when only one form of a redox couple is adsorbed on the electrode surface to prevent inner-sphere and self-exchange ET, as we claimed for the first time in recent studies of ferrocene derivatives at HOPG [104, 111]. In this case, only the reduced form of ferrocene derivatives is adsorbed on the HOPG surface ($\Gamma_{O,s}\beta_O << \Gamma_{R,s}\beta_R$) to thermodynamically decouple outer-sphere oxidation of the reduced form and suppress its inner-sphere oxidation ($E^{0\prime}_{IS} >> E^{0\prime}_{OS}$ in Eq. (1.10)). Coupling of surface adsorption with outer-sphere oxidation was clearly demonstrated by CV, where a forward peak was enhanced much more at a

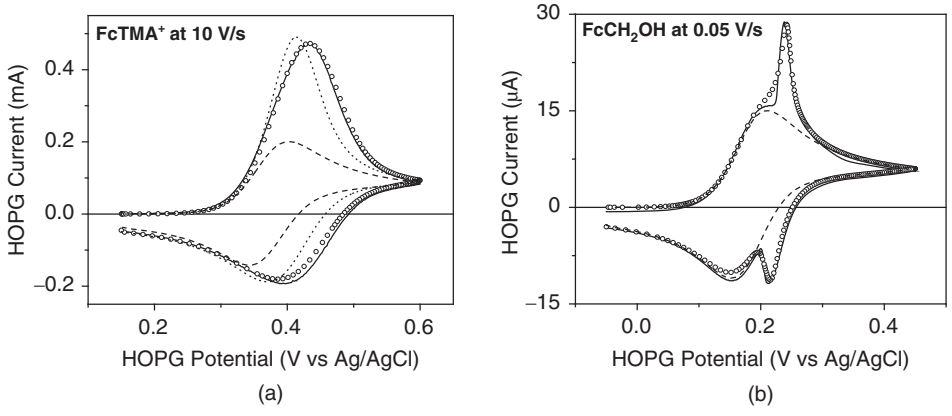

Figure 1.7 Background-subtracted experimental CVs (solid lines) of 0.3 mM (a) $FcTMA^+$ at 10 V s^{-1} and (b) $FcCH_2OH$ at 0.05 V s^{-1} with water-protected HOPG in 1 M KCl. Theoretical CVs were simulated with the best fit (circles), no adsorption (dashed lines), and previously reported parameters [110] (dotted line only in part A). Source: Reprinted with permission from Kurapati et al. [111]. Copyright 2018 American Chemical Society.

faster scan rate than the reverse peak (e.g. $FcTMA^+$ at 10 V s^{-1} in Figure 1.7a [111]). The enhancement of the forward peak proves that the reduced form of ferrocene derivatives was desorbed from the HOPG surface to participate in outer-sphere oxidation. A lower reverse peak indicates the lack of adsorption of the oxidized form of ferrocene derivatives, e.g. $FcTMA^{2+}$. In fact, experimental CV was fitted very well with CV simulated by considering only outer-sphere ET coupled with surface adsorption of the reduced form of ferrocene derivatives (Figure 1.7a). The best fit required the consideration of intermolecular interactions among adsorbed ferrocene derivatives, which was implemented by employing the Frumkin isotherm based on Bragg–Williams approximation [123] to yield [124]

$$\beta_i C_i(0,t) = \frac{\Gamma_i}{\Gamma_{i,s} - \Gamma_i} \exp\left(-g_i' \frac{\Gamma_i}{\Gamma_{i,s}}\right) \tag{1.13}$$

where only one species, i, is adsorbed and g_i' represents interactions among adsorbates on the electrode surface. Weak electrostatic repulsion among adsorbed $FcTMA^+$ yielded a small negative g_i' value of -0.3 ± 0.2, which corresponds to a wider forward peak than expected from the Langmuir isotherm ($g_i' = 0$). Experimental CVs at various scan rates consistently fitted with CVs simulated by using the Frumkin isotherm with $\log\beta_i$ ($l\,mol^{-1}$) $= 3.6 \pm 0.3$ and $\Gamma_{i,s} = (1.8 \pm 0.5) \times 10^{-10}$ mol cm^{-2}. A good fit was not obtained with CV simulated by using previously reported parameters, i.e. the Langmuir isotherm with $\log\beta_i$ ($l\,mol^{-1}$) $= 2.9$ and $\Gamma_{i,s} = 5.0 \times 10^{-10}$ mol cm^{-2} [110], which was overestimated by incorrectly assuming that the cyclopentadienyl ring of $FcTMA^+$ was closely packed on the HOPG surface despite the substituent.

Interestingly, $FcCH_2OH$ was adsorbed strongly on the water-protected HOPG surface in low TOC ultrapure water to yield a pair of adsorption-based post peaks (Figure 1.7b). Such a pair of post peaks was not reported in previous CV studies [55, 115, 125], perhaps because HOPG was not protected from organic contamination in ambient air or ultrapure water. Importantly, the post peaks are attributed to the

coupling between outer-sphere ET and surface adsorption of $FcCH_2OH$, not to inner-sphere ET of adsorbed forms of the $FcCH_2OH^{+/0}$ couple. In fact, CVs simulated with adsorption-coupled outer-sphere ET yielded good fits with experimental CVs at up to $10\,V\,s^{-1}$, where post peaks merged with diffusional peaks. The resultant CV with a much higher forward peak characteristically indicates that only $FcCH_2OH$ was adsorbed on the HOPG surface to mediate only outer-sphere ET. The weak dependence of reverse peak on scan rate is inconsistent with inner-sphere ET of an adsorbed redox couple [47], where both forward and reverse peaks vary proportionally with the scan rate. It should be emphasized that a pair of post (or pre) peaks coupled with a pair of diffusional peaks was simulated by Wopschall and Shain [126], who considered only outer-sphere ET and the adsorption of a reactant (or a product), although their work was cited recently to attribute a pair of pre peaks to inner-sphere ET of an adsorbed redox couple [127]. Similarly, Speiser and coworkers considered only outer-sphere ET coupled with Langmuir [128] or Frumkin [129] adsorption of a redox couple to simulate a pair of adsorption-based peaks preceding or following a pair of diffusional peaks. We are unaware of any theoretical work that yielded a pair of diffusional peaks preceded or followed by a pair of peaks based on inner-sphere ET.

The strong adsorption of $FcCH_2OH$ on the HOPG surface is attributed to strong intermolecular interactions among adsorbed $FcCH_2OH$ as demonstrated by the highly positive g_i' value of $+3.2 \pm 0.3$ determined by the finite element analysis of CV. The strong intermolecular interactions are attributed to hydrogen bonding and qualitatively represented by the narrow widths of not only post peaks at low scan rate (Figure 1.7b), but also higher forward peaks at faster scan rates. By contrast, $\Gamma_{i,s} = (3.0 \pm 0.6) \times 10^{-10}\,mol\,cm^{-2}$ and $\log\beta_i\,(l\,mol^{-1}) = 3.7 \pm 0.1$ for $FcCH_2OH$ are similar to those of $FcTMA^+$ (see above). Overall, free energy changes for the entire adsorption step, $\Delta\overline{G^0}$, of $FcCH_2OH$ ($-30 \pm 1\,kJ\,mol^{-1}$) is more negative than those of $FcTMA^+$ ($-21 \pm 2\,kJ\,mol^{-1}$), because free energy changes for intermolecular interactions among adsorbed $FcCH_2OH$ ($-8.0 \pm 0.7\,kJ\,mol^{-1}$) are more negative than $FcTMA^+$ ($+0.7 \pm 0.4\,kJ\,mol^{-1}$), i.e. $-RTg_i'$ at saturation ($\Gamma_i/\Gamma_{i,s} = 1$), as given by [124]

$$\Delta\overline{G^0} = -RT\ln\beta_i - RTg_i'(\Gamma_i/\Gamma_{i,s}) \tag{1.14}$$

where free energy changes for interactions with HOPG, i.e. $-RT\ln\beta_i$, are similar between $FcCH_2OH$ ($-21.5 \pm 0.8\,kJ\,mol^{-1}$) and $FcTMA^+$ ($-21 \pm 2\,kJ\,mol^{-1}$). Moreover, adsorption isotherms can be plotted using adsorption parameters determined from CVs to find adsorption strength in the order of $FcCH_2OH$ > 1,1′-ferrocenedimethanol, $Fc(CH_2OH)_2$, > $FcTMA^+$ (Figure 1.8a). The adsorption of $FcTMA^+$ is underestimated by using a Langmuir isotherm with an overestimated $\Gamma_{i,s}$ value and an underestimated $\log\beta_i$ value, as reported previously [110].

Adsorption parameters are obtainable by CV, which represents the adsorption isotherm as illustrated by simulating concentrations of redox couples at OHP and IHP of HOPG against its potential (e.g. $FcCH_2OH$ in Figure 1.8b). At the initial potential of −0.05 V, the HOPG surface is nearly saturated with $FcCH_2OH$ (solid red line). As the potential is scanned to >0.1 V, $FcCH_2OH$ at the OHP (solid blue line) is oxidatively consumed to generate $FcCH_2OH^+$ at the OHP (solid black line). The HOPG surface, however, is still nearly saturated with $FcCH_2OH$, which is strongly adsorbed even when the concentration of $FcCH_2OH$ at the OHP is lowered to ~40% of the bulk concentration at 0.2 V. More positive potentials of >0.3 V are required to significantly

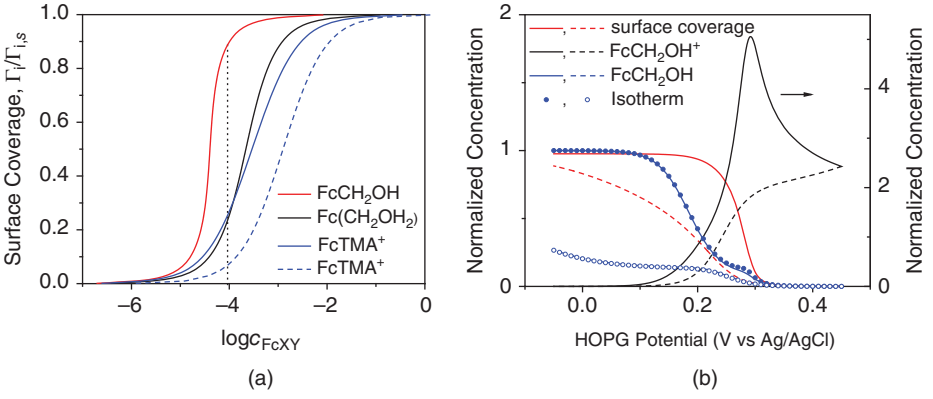

Figure 1.8 (a) Adsorption isotherms (solid lines) for ferrocene derivatives on HOPG in 1 M KCl as calculated by using β_i and g_i' values determined from CVs (e.g. Figure 1.7). Dashed line represents the adsorption isotherm of $FcTMA^+$ misestimated in the previous study. Vertical dotted line indicates the concentration of 0.3 mM ferrocene derivatives used for CV. (b) Normalized concentrations of the $FcCH_2OH^{+/0}$ couple at HOPG as simulated for 0.3 mM $FcCH_2OH$ in 1 M KCl by employing a scan rate of 10 V s^{-1} and parameters determined from the corresponding CV. Solid lines and closed circles represent the forward scan. Dashed lines and open circles correspond to the reverse scan. Source: Reprinted with permission from Kurapati et al. [111]. Copyright 2018 American Chemical Society.

desorb $FcCH_2OH$ from the HOPG surface to significantly enhance the current response based on the oxidation of desorbed $FcCH_2OH$ at the OHP, where the concentration of $FcCH_2OH^+$ exceeds the bulk concentration of $FcCH_2OH$ by a factor of ~5. Eventually, the switching potential of 0.45 V is positive enough to completely deplete $FcCH_2OH$ at both OHP and IHP, but still maintain a high concentration of $FcCH_2OH^+$ at the OHP. The concentration of $FcCH_2OH$ adsorbed on the IHP is nearly recovered to saturation during the reverse scan, where $FcCH_2OH$ at the OHP is still largely depleted owing to the strong and fast adsorption of $FcCH_2OH$ on the IHP. The equilibrium adsorption of $FcCH_2OH$ is maintained during the entire potential scan, as demonstrated by the good agreement between the simulated $FcCH_2OH$ concentration at the OHP and the concentration of $FcCH_2OH$ at the OHP calculated using the Frumkin isotherm with the simulated concentration of $FcCH_2OH$ on the IHP (circles in Figure 1.8b).

1.6 Self-Inhibition of Outer-Sphere ET

A redox-active molecule can be adsorbed on the electrode surface to self-inhibit outer-sphere ET, as revealed by SECM-based NV in our recent study [130]. Specifically, a self-inhibitory effect was observed by SECM-based NV of $Co(phen)_3^{2+}$, which was adsorbed on the eC surface to electrostatically block the access of non-adsorbed $Co(phen)_3^{2+}$ and $Co(phen)_3^{3+}$ to the OHP (Figure 1.9a). Heterogeneous ET of the $Co(phen)_3^{3+/2+}$ couple at the eC surface was mediated unambiguously by an outer-sphere pathway, because only $Co(phen)_3^{2+}$ was adsorbed on the eC surface as confirmed by CV and SECM-based NV. The self-inhibitory effect was less serious in the SG/TC mode, where $Co(phen)_3^{2+}$ was oxidatively consumed at the OHP to desorb the blocking adsorbates. Moreover, weak electrostatic repulsion was exerted on the access

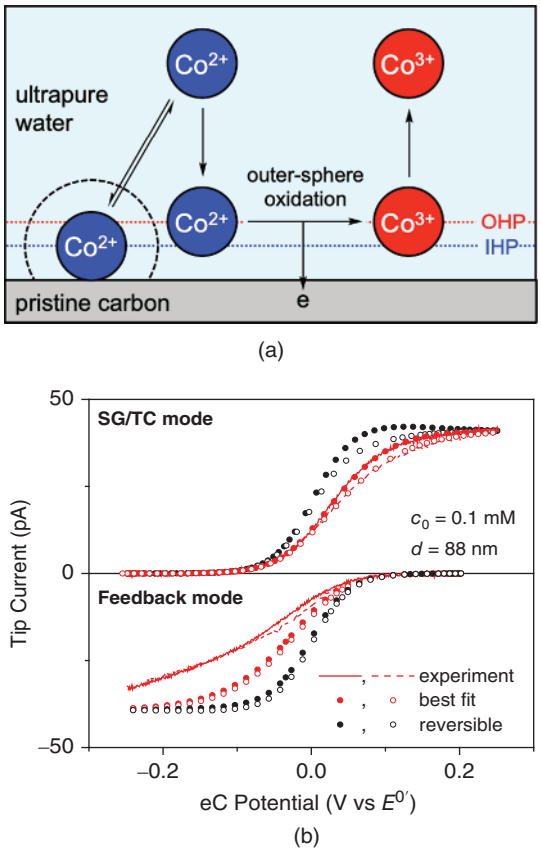

Figure 1.9 (a) Self-inhibition of $Co(phen)_3^{2+}$ oxidation by $Co(phen)_3^{2+}$ adsorbed on the eC surface. (b) Experimental (lines) and simulated (circles) nanogap voltammograms of 0.1 mM ($= c_0$) $Co(phen)_3^{2+}$ at an eC electrode in 1 M KCl as obtained by using a 0.80 μm-diameter Pt tip in SG/TC (top) and feedback (bottom) modes. Potential sweep rate, 0.05 V s^{-1}. A tip–eC distance, d, 88 nm. Open and closed circles are forward and reverse scans, respectively. Solid and dashed lines are the respective scans. Source: Reprinted with permission from Chen et al. [130]. Copyright 2018 American Chemical Society.

of less charged $Co(phen)_3^{2+}$ to the OHP in the SG/TC mode. The resultant SECM-based NV was fitted well with simulated NV to yield a k^0 value (0.217 cm s^{-1} with 0.1 mM $Co(phen)_3^{2+}$ in the top panel of Figure 1.9b) and a α value of 0.5 as expected from the Marcus theory. The adsorption of only $Co(phen)_3^{2+}$ at the IHP of the eC surface was ensured by the hysteresis of the NV, where the tip current was enhanced only during the forward scan by the oxidation of $Co(phen)_3^{2+}$ desorbed from the eC surface to yield no enhancement during the reverse scan. A good fit of experimental and simulated hysteresis yielded $\Gamma_{i,s} = 3.8 \times 10^{-11}$ mol cm^{-2} and $\log\beta_i$ (l mol^{-1}) = 5.2 in addition to a large negative g'_i value of −4.6, which indicates strong electrostatic repulsion among adsorbed $Co(phen)_3^{2+}$ molecules. By contrast, a good fit was not obtainable for SECM-based NV in the feedback mode (the bottom panel of Figure 1.9b), where $Co(phen)_3^{2+}$ was generated and adsorbed on the eC surface to seriously self-inhibit the access of highly charged $Co(phen)_3^{3+}$ to the OHP for outer-sphere reduction. SECM-based NVs in the feedback mode were too board to fit with NVs simulated by using optimized parameters for the SG/TC branches or any set of parameters including a α value of 0.5 as expected for outer-sphere ET. Advantageously, the self-inhibitory oxidation of $Co(phen)_3^{2+}$ was irreversible under high mass-transport conditions across nanogaps to yield NVs without an effect of seriously self-inhibitory reduction of $Co(phen)_3^{3+}$, thereby following the Marcus theory as evidenced by an α value of 0.5.

A self-inhibitory effect on $Co(phen)_3^{2+}$ oxidation was quantitatively characterized and explained by extending the Amatore model of partially blocked electrodes [131–133]. Adsorbed $Co(phen)_3^{2+}$ molecules blocked the eC surface to reduce a fraction of the bare eC surface to $1 - \theta_i$, where $\theta_i = \Gamma_i/\Gamma_{i,s}$. In addition, the access of $Co(phen)_3^{2+}$ to the OHP of the bare eC surface was electrostatically inhibited by adsorbates to yield an effective fraction of $1 - \theta_i\gamma$, where γ represents the electrostatic blocking effect from adsorbates to extend the Amatore model to self-inhibitory ET, i.e.

$$k^0 = k^0_{OS}\,[1 - \theta_i\gamma] \tag{1.15}$$

This relationship was quantitatively ensured by plotting k^0 against θ_i at $E^{0'}$ for $Co(phen)_3^{2+}$ oxidation at the eC surface as determined by the finite element analysis of SECM-based NV. Experimentally, the bulk concentration of $Co(phen)_3^{2+}$ in 1 M KCl was increased from 0.05 to 1 mM to increase θ_i at $E^{0'}$ from ~0.4 to ~0.8. The corresponding k^0 values linearly decreased to yield $k^0_{OS} = 0.60$ cm s^{-1} at $\theta = 0$ and $\gamma = 1.29$ from the slope. The concentration dependence of k^0 is anomalous and apparently inconsistent with the Marcus theory, but is accountable by considering the self-inhibitory mechanism. It should be noted that self-inhibitory effects on heterogeneous ET have also been known as autoinhibition in classical polarography [134], but is rarely discussed in modern electrochemistry. More recently, Bard and coworkers employed SECM to suggest a self-inhibitor effect at a Pt UME tip, where both $FcCH_2OH$ and $FcCH_2OH^+$ were adsorbed from a mixture of water and dimethyl sulfoxide (DMSO) to yield low k^0 values of ~0.28 cm s^{-1} [135].

We also employed SECM-based CV with micrometer gaps [136] to discover the importance of surface adsorption and self-inhibitory ET in the multistep electrodeposition of a multielement material, magnetite, Fe_3O_4. This mechanistic study is significant, because magnetite [137] is a multifunctional compound that is attractive for magnetic memory devices [138–140], electrocatalysis [141–143], and lithium-ion batteries [144]. Specifically, we found that the well-established electrodeposition of magnetite from an alkaline solution of Fe(III)–triethanolamine (TEA) [145] can be preceded by the reductive generation and following adsorption of Fe(II)–TEA on the Au substrate surface. Importantly, the adsorbed Fe(II) intermediate was unresolvable from co-deposited Fe_3O_4 in situ by other electrochemical techniques and was readily oxidized in air and undetectable by ex-situ spectroscopy and microscopy [145]. The adsorbed intermediate was identified through the quantitative analysis of complicated, but highly informative SECM-based CVs. In the SG/TC mode, the substrate potential was scanned to the negative direction, where Fe(II)–TEA was reductively generated from Fe(II)–TEA, adsorbed on the substrate, and converted to magnetite to lower a tip current based on the oxidation of Fe(II)–TEA (the bottom panel of Figure 1.10). The tip current was lowered further during the reverse scan owing to the further deposition of magnetite and was not recovered even at positive potentials, where Fe(II)–TEA was produced by the electrodissolution of magnetite, but was immediately oxidized to Fe(III)–TEA. By contrast, the tip current based on the reduction of Fe(III)–TEA in the feedback mode was largely enhanced by the electrodissolution of magnetite during the reverse scan to yield a transient peak response in addition to a sigmoidal quasi-steady-state response (the top panel of Figure 1.10). It should be noted that SECM-based CV with micrometer-gaps tend to yield larger transient responses based on surface adsorption and desorption in comparison with SECM-based NV as

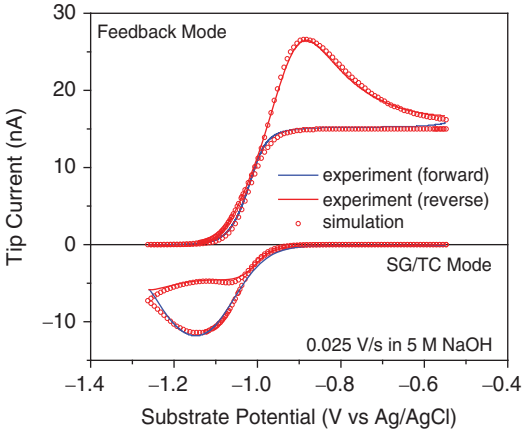

Figure 1.10 Experimental (solid lines) and simulated (circles) SECM-based CVs in feedback (top) and SG/TC (bottom) modes with a 25 μm-diameter Au tip over a 2 mm-diameter Au substrate in a 5 M NaOH solution containing 5 mM Fe(III)–TEA. Tip potentials, −1.12 and −0.75 V vs Ag/AgCl for the respective operation modes. Potential sweep rate, 0.025 V s^{-1}. Switching potential, −1.26 V vs Ag/AgCl. Source: Reprinted with permission from Bhat et al. [136]. Copyright 2017 American Chemical Society.

demonstrated for adsorption-coupled outer-sphere oxidation of $FcTMA^+$ on HOPG [110] and electrosorption of hydrogen on Pt electrodes [146, 147].

Advantageously, eight parameters for the three-step deposition of magnetite were determined precisely by the finite element analysis of the amperometric tip current free from the background response, thereby eliminating the need for background subtraction. A large $\Gamma_{i,s}$ value of 5.4×10^{-9} mol cm^{-2} indicates that the multiple layers of Fe(II)–TEA and, subsequently, magnetite were deposited. Moreover, the adsorption of Fe(II)–TEA was strong, not only because of strong interactions between Fe(II)–TEA and the substrate with $\log\beta_i$ (l mol^{-1}) = 5.2, but also because of strong attractive interactions among adsorbates with $g_i' = +3.3$, which was attributed to the adsorption and conversion of Fe(II)–TEA to an oxide or a hydroxide. In contrast to conductive magnetite, insulating oxide and hydroxide self-inhibited outer-sphere ET of the Fe(III/II)–TEA couple, which was considered in the finite element analysis to improve a fit between experimental and simulated voltammograms.

1.7 Coupling Between Outer- and Inner-Sphere ET

Here we consider a model based on simultaneous outer- and inner-sphere ET (Figure 1.1) when both forms of a redox couple are similarly adsorbed on the electrode surface to yield $\Gamma_{O,s}\beta_O = \Gamma_{R,s}\beta_R = \Gamma_s\beta$ and, subsequently, $E_{IS}^{0'} = E_{OS}^{0'} = E^{0'}$ in Eq. (1.10), thereby coupling both pathways thermodynamically. Moreover, steady-state [21, 40, 41] and transient [21, 23, 42] voltammetry were considered theoretically to conclude that outer- and inner-sphere pathways are indistinguishable kinetically when adsorption equilibrium is maintained. This conclusion implies a paradox that the resultant voltammetric wave resembles that of only outer-sphere ET coupled with mass transport even when inner-sphere ET is exclusive [22], thereby missing signatures of adsorption phenomena, which we call the Laviron–Amatore paradox. Alternatively, only adsorption waves based on inner-sphere ET may be obtainable to miss information about outer-sphere ET owing to the paradox [42] when desorption kinetics is much slower than the time scale of electrochemical measurements. Here, we justify the Laviron–Amatore paradox by considering the kinetic convolution of

outer- and inner-sphere ET as reported in our recent work [148]. When ET is mediated through both pathways, the overall ET rate, v, is given by

$$v = v_{OS} + v_{IS} \tag{1.16}$$

where v_{OS} and v_{IS} are rates of outer- and inner-sphere ET, respectively. The extended Amatore model of self-inhibitory outer-sphere ET yields [130, 148]

$$v_{OS} = (1 - \theta_O - \theta_R)[k_{OS}^{red} C_O(0, t) - k_{OS}^{ox} C_R(0, t)] \tag{1.17}$$

with

$$k_{OS}^{red} = k_{OS}^0 \exp\left[-\frac{\alpha_{OS} F(E - E_{OS}^{0'})}{RT}\right] \tag{1.18}$$

$$k_{OS}^{ox} = k_{OS}^0 \exp\left[\frac{(1 - \alpha_{OS}) F(E - E_{OS}^{0'})}{RT}\right] \tag{1.19}$$

Moreover, v_{IS} is given by [21]

$$v_{IS} = k_{IS}^{red} \Gamma_O - k_{IS}^{ox} \Gamma_R \tag{1.20}$$

with

$$k_{IS}^{red} = k_{IS}^0 \exp\left[-\frac{\alpha_{IS} F(E - E_{IS}^{0'})}{RT}\right] \tag{1.21}$$

$$k_{IS}^{ox} = k_{IS}^0 \exp\left[\frac{(1 - \alpha_{IS}) F(E - E_{IS}^{0'})}{RT}\right] \tag{1.22}$$

When $\alpha_{OS} = \alpha_{IS} = \alpha$ (~0.5) and $\beta_O = \beta_R = \beta$ (and, accordingly, $\Gamma_{O,s} = \Gamma_{R,s} = \Gamma_s$), a combination of Eqs. (1.16)–(1.22) yields

$$v = k^0 \left\{ c_O(0, t) \exp\left[-\frac{\alpha F(E - E^{0'})}{RT}\right] - c_R(0, t) \exp\left[\frac{(1 - \alpha) F(E - E^{0'})}{RT}\right] \right\} \tag{1.23}$$

with

$$k^0 = \frac{k_{OS}^0 + \beta \Gamma_s k_{IS}^0}{1 + \beta c_0} \tag{1.24}$$

where c_0 is the total bulk concentration of the redox couple and $C_O(0, t) + C_R(0, t) = c_0$ is assumed owing to similar adsorptivities of oxidized and reduced forms in contrast to earlier examples where the reduced (or oxidized) form was adsorbed more strongly (Figure 1.8b). Overall, Eqs. (1.23) and (1.24) support the Laviron–Amatore paradox that outer- and inner-sphere ET is unresolvable when adsorption equilibrium is maintained for both forms of a redox couple with similar adsorptivities. Equation (1.23) shows that v is equivalent to v_{OS} when k^0 is replaced with k_{OS}^0, thereby predicting voltammetric responses without a feature of inner-sphere ET. Moreover, Eq. (1.24) ensures that k_{OS}^0 and k_{IS}^0 are not separately determinable from an experimentally measurable k^0 value.

Recently, we proposed [73] that coupling between outer- and inner-sphere ET may be a reason why high k^0 values of the $Ru(NH_3)_6^{3+/2+}$ couple determined by various nanoelectrochemical methods (Table 1.3) exceed the highest possible k_{OS}^0 value of 2.2 cm s^{-1}

Table 1.3 Standard ET rate constants of $Ru(NH_3)_6^{3+}$ at carbons and metals.

Electrode	k^0 (cm s^{-1})	Method	Note	Ref.
—	2.2	—	Marcus theory	[149]
Pt nanoparticle	36 ± 4	Voltammetry	Low-TOC water	[150]
Carbon nanoelectrode	≥ 10	Voltammetry	Low-TOC water	[91]
eC (KCl protection)	≥ 6.9	SECM	Low-TOC water	[73]
eC	1.7 ± 0.2	SECM	Low-TOC water	[73]
CF	0.9	Voltammetry	Low-TOC water	[148]
SWCNT	4 ± 2	SECCM	Ambient air	[106]
SWCNT (metallic)	10 ± 5	SECCM	Ambient air	[107]
Glassy carbon	≥ 2.0	AC voltammetry		[151]
Pt nanoelectrode	79 ± 44	Voltammetry		[97]
Pt nanoelectrode	17.0 ± 0.9	Voltammetry		[94]
Au nanoelectrode	13.5 ± 2	Voltammetry		[95]

predicted by the Marcus theory for adiabatic outer-sphere ET [149]. For instance, theoretical k^0 values based on Eq. (1.24) increase up to 46 cm s^{-1} for the $Ru(NH_3)_6^{3+/2+}$ couple by using $k_{IS}^0 = 5.39 \times 10^6$ s^{-1} and $\Gamma_s = 1.5 \times 10^{-10}$ mol cm^{-2} for the monolayer of $HS(CH_2)_3$(pyridine)Ru-$(NH_3)_5^{3+}$ [152] and $\beta = 5.39 \times 10^4$ cm^3 mol^{-1} for $Ru(NH_3)_6^{3+}$ [153] at Au electrodes. More specifically, Eq. (1.24) with $c_0 = 5$ mM yields a slightly lower k^0 value of 36 cm s^{-1}, which agrees very well with a k^0 value of 5 mM $Ru(NH_3)_6^{3+}$ at single Pt nanoparticles [150]. Importantly, the Pt nanoparticles were investigated in low-TOC water, which also yielded diffusion-limited minimum k^0 values of ≥ 10 and ≥ 6.9 cm s^{-1} at carbon nanoelectrodes and KCl-protected eC electrodes to exceed the Marcus prediction and also include the predictions based on Eq. (1.24). Low-TOC water yielded a low and finite k_0 value of 0.90 cm s^{-1} at carbon-fiber (CF) UMEs, which was not electrochemically activated and was also exposed to ambient air as well as Ga^+ and electron beams for electrode fabrication. In fact, the low k^0 value at CF UMEs was similar to that of non-protected eC electrodes in low-TOC water [73]. Similarly, the Marcus prediction of 2.2 cm s^{-1} was exceeded also at nanoelectrodes made of Pt [94] and Au [95], where both $Ru(NH_6)_3^{3+}$ and $Ru(NH_6)_3^{2+}$ are adsorbed [153, 154]. The finite k^0 values, however, were limited to ~15 cm s^{-1} and lower than predicted by Eq. (1.24), perhaps because nanoelectrodes were quickly contaminated owing to fast mass transport of organic impurities in ultrapure water purified only by filtrations [65]. Similarly, k^0 values of single SWCNTs were higher than the Marcus prediction, but were lower than expected from Eq. (1.24), perhaps because these k^0 values were measured by SECCM of SWCNTs exposed to ambient air [106, 107]. It should be noted that high k^0 values of 79 ± 44 cm s^{-1} were overestimated by using recessed Pt nanoelectrodes [97], which may be attributed to electrostatic damage [84]. AC voltammetry was too slow to determine a k^0 value of higher than 2 cm s^{-1} at glassy carbon electrodes [151], where both $Ru(NH_6)_3^{3+}$ and $Ru(NH_6)_3^{2+}$ are adsorbed [155] to mediate both outer- and inner-sphere ET.

It should be noted that Eq. (1.24) is similar to the equation proposed by Anson [29] to account for the non-linear concentration dependence of exchange current, i_0, [30] by assuming both outer- and inner-sphere ET of the $Fe^{3+/2+}$ couple at the Pt electrode, i.e.

$$i_0 = nF[k^0_{OS}C + k^0_{IS}\Gamma_s x^{\alpha_{IS}}(1-x)^{1-\alpha_{IS}}] \tag{1.25}$$

where C is the equal bulk concentration of Fe^{3+} and Fe^{2+}, and x is the fraction of adsorbed Fe^{3+}. Equation (1.25) is not identical to Eq. (1.24), because Anson did not consider a specific adsorption isotherm or the self-inhibition of outer-sphere ET by adsorbates. Interesting, Brown and Anson employed the Marcus theory to estimate [37]

$$k^0_{IS} = 6 \times 10^8 k^0_{OS} \tag{1.26}$$

where k^0_{OS} and k^0_{IS} have units of s^{-1} and cm s^{-1}, respectively, both outer- and inner-sphere ET are adiabatic and have the identical reorganization energy, and a pre-exponential factor of inner-sphere ET is given by kT/h. Laviron proposed a larger coefficient for $k^0_{IS} = 2 \times 10^9 k^0_{OS}$ [40, 42] from the expression derived by Mohilner using the Marcus theory [156]. Equation (1.24) for the $Ru(NH_3)_6^{3+/2+}$ couple [73] employed a k^0_{IS} value of $5.39 \times 10^6\ s^{-1}$ for the monolayer of $HS(CH_2)_3$(pyridine)Ru-$(NH_3)_5^{3+}$ [152], which was much smaller than a k^0_{IS} value of $1.3 \times 10^9\ s^{-1}$ expected from Eq. (1.26) with $k^0_{OS} = 2.2\ cm\ s^{-1}$. The k^0_{IS} values are very different, potentially because the k^0_{IS} value of $HS(CH_2)_3$(pyridine)Ru-$(NH_3)_5^{3+}$ self-assembled on the Au electrode was lowered by electron tunneling through the spacer between the ruthenium redox center and the electrode surface [152] to represent nonadiabatic ET. Moreover, k^0_{IS} may be overestimated for the $Ru(NH_3)_6^{3+/2+}$ couple by Eq. (1.26), because the pre-exponential factor was determined for inner-sphere ET of 9,10-phenanthrolinequinone and because adiabatic mechanisms and identical reorganization energies were assumed for outer- and inner-sphere ET [37]. Attempts have been made to theoretically assess pre-exponential factor [157] and reorganization energy [158]. The latter predicted that the reorganization energy of *p*-dicyanobenzene was lower at the IHP than at the OHP to accelerate inner-sphere ET by a factor of ~10. The lower reorganization energy of an adsorbed redox species has been suggested, e.g. by Gerisher [159] and McCreery [160].

Outer- and inner-sphere ET can be coupled also through a heterogeneous self-exchange reaction (Eq. (1.5)), which is unimportant when equilibrium adsorption is maintained for both oxidized and reduced forms of a redox couple [23, 112] (Figure 1.11a) or when both outer- and inner-sphere ET are reversible [112] (Figure 1.11b). We obtained this conclusion generally by using electrochemical potentials without specific expressions for heterogeneous ET or surface adsorption [112], which was somehow misrepresented in a recent article [89]. The electrochemical

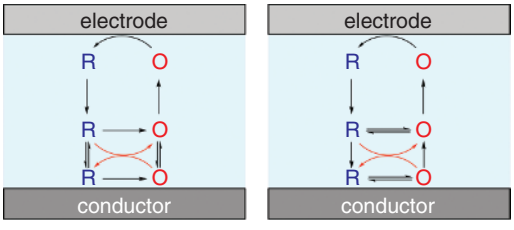

Figure 1.11 Heterogeneous self-exchange ET at conductor with (a) equilibrium adsorption steps or (b) reversible ET steps. Red arrows indicate the forward reaction of Eq. (1.5). Source: Reprinted with permission from Amemiya [112]. Copyright 2017 American Chemical Society.

potential of species i, $\overline{\mu}_i$, is defined for both adsorbed and non-adsorbed forms of a redox couple without the need of an adsorption isotherm. The rate of a self-exchange reaction is zero when both of adsorption steps are at equilibrium (i.e. $\overline{\mu}_O = \overline{\mu}_{O_{ads}}$ and $\overline{\mu}_R = \overline{\mu}_{R_{ads}}$ [161]) or when both of ET steps are reversible (i.e. $\overline{\mu}_O + \overline{\mu}_e = \overline{\mu}_R$ and $\overline{\mu}_{O_{ads}} + \overline{\mu}_e = \overline{\mu}_{R_{ads}}$ [162], where $\overline{\mu}_e$ is the electrochemical potential of electron), because the net electrochemical potentials are identical for reactants and products of a self-exchange reaction as given by

$$\overline{\mu}_{O_{ads}} + \overline{\mu}_R = \overline{\mu}_{R_{ads}} + \overline{\mu}_O \tag{1.27}$$

Accordingly, it is a misconception that a self-exchange reaction is important in the model of ET kinetics based on equilibrium adsorption [55]. By contrast, adsorption isotherms, e.g. Langmuir isotherms for competitive adsorption (Eqs. (1.6) and (1.7)), can be used to calculate the equilibrium constant of self-exchange reaction, K_{ex}, to yield [112]

$$K_{ex} = \exp\left[\frac{nF(E^{0'}_{IS} - E^{0'}_{OS})}{RT}\right] = \frac{\Gamma_{R,s}\beta_R}{\Gamma_{O,s}\beta_O} \tag{1.28}$$

This equation reconfirms that the equilibrium of the self-exchange reaction is determined by the equilibrium of heterogeneous ET and surface adsorption and is independent of electrode potential. Moreover, Eq. (1.28) gives $K_{ex} = 1$ when outer and inner-sphere ET occurs simultaneously with $\Gamma_{O,s}\beta_O = \Gamma_{R,s}\beta_R = \Gamma_s\beta$ and, subsequently, $E^{0'}_{IS} = E^{0'}_{OS} = E^{0'}$ in Eq. (1.5). In this case, forward and reverse rate constants, k^{ex}_f and k^{ex}_b, respectively, of the self-exchange reaction are identical, because of $K_{ex} = k^{ex}_f / k^{ex}_b$.

A self-exchange reaction can be kinetically controlled and distinguished from other steps only when at least one of adsorption steps and one of ET steps is kinetically controlled [112]. Importantly, Anson indicated that a self-exchange reaction is a second-order reaction and can be kinetically distinguished from outer- and inner-sphere ET [29]. Quantitatively, the corresponding rate of self-exchange reaction, v_{ex}, is given by

$$v_{ex} = k^{ex}_f \Gamma_O C_R(0,t) - k^{ex}_b \Gamma_R C_O(0,t) \tag{1.29}$$

where Γ_O and Γ_R also vary with $C_O(0, t)$ and $C_R(0, t)$, respectively, to follow the second-order kinetics. The self-exchange reaction does not directly contribute to a current response in contrast to outer- and inner-sphere ET. The self-exchange reaction, however, is still relevant, because it affects concentrations of a redox couple on and near the electrode surface. DuVall and McCreery proposed that dopamine (DA) oxidation to dopamine-*o*-quinone (DOQ) can be medicated through not only an inner-sphere pathway, but also a self-exchange pathway [163] (Figure 1.12).

1.8 Resolving Outer- and Inner-Sphere ET

Attempts were made to resolve outer- and inner-sphere ET of a redox couple, and, subsequently, determine k^0_{OS} and k^0_{IS} values separately. For instance, Laviron employed fast-scan CV [42] to determine k^0_{IS} values from surface waves [164] for small aromatic molecules adsorbed on mercury electrodes in the aqueous media [165–168]. In these studies, k^0_{OS} values were not determinable, because both outer- and inner-sphere ET

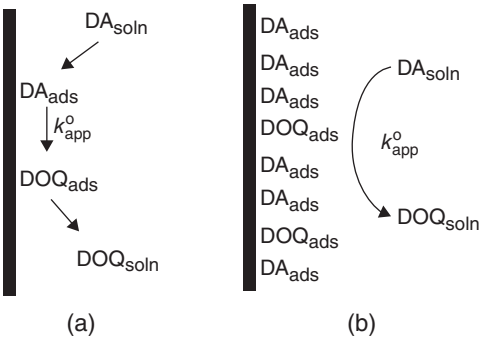

Figure 1.12 Schematic models for adsorption-dependent oxidation of DA to DOQ through (a) inner-sphere and (b) self-exchange pathways with apparent standard rate constants, k^o_{app}. Source: Reprinted with permission from DuVall and McCreery [163]. Copyright 2000 American Chemical Society.

were driven simultaneously owing to similar adsorptivities of oxidized and reduced forms [42], i.e. $E^{0'}_{IS} \approx E^{0'}_{OS}$, and were unresolvable at slow scan rates. Accordingly, k^0_{OS} values were measured without surface adsorption in the non-aqueous media and used in Eq. (1.26) to yield k^0_{IS} values that were similar to those measured in the aqueous media. More recently, Amatore and coworkers employed fast-scan CV to resolve outer- and inner-sphere pathways for the reduction of benzyl chloride at silver electrodes [22]. In this study, k^0_{OS} and k^0_{IS} values were separately determinable, because the corresponding voltammetric waves were observed at separate potentials (~0.6 V) when the scan rate was fast enough. We are unaware of any report where outer- and inner-sphere ET that occur at similar potentials were resolved, which is possible in principle when adsorption equilibrium is not maintained.

Recently, we investigated DA oxidation by fast-scan NV based on double-CF UMEs with a nanometer-wide gap [148] (Figure 1.13), which may serve as a powerful approach to resolve outer- and inner-sphere ET. Double-CF UMEs were originally developed to improve the time resolution of NV by employing fast scan rates of up to 100 V s^{-1}, which is ~1000 times faster than reported with any nanogap-based electrochemical cell (i.e. ≤0.1 V s^{-1} [33]). We simulated fast scan NV at double-cylinder UMEs with a nanometer-wide gap as a model of two CFs sealed in a glass capillary [169]. Simulated NVs fitted well with experimental NVs based on voltammetric responses to $Ru(NH_3)_6^{3+}$ at a CF generator electrode and amperometric responses to $Ru(NH_3)_6^{2+}$ at a CF collector electrode at up to 100 V s^{-1} to determine consistent gap widths of ~0.18 μm and a k^0 value of 0.9 cm s^{-1} (Table 1.3). Advantageously, a transient background response of amperometric collector electrode was suppressed ~100 times in comparison with that

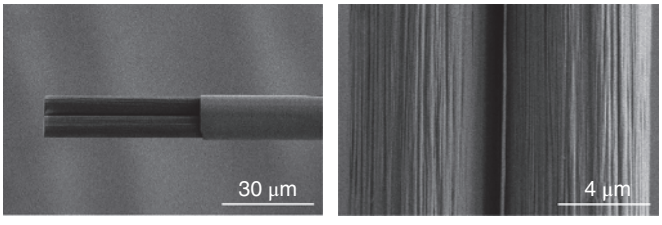

Figure 1.13 Scanning electron microscopy of (a) a double-CF UME sealed in a glass capillary and (b) a nanogap between CFs. Source: Reprinted with permission from Pathirathna et al. [148]. Copyright 2018 American Chemical Society.

of the voltammetric generator electrode, thereby eliminating the need for background subtraction for quantitative data analysis.

Double-CF UMEs voltammetrically oxidize DA at a generator electrode to produce DOQ, which is amperometrically detected at a collector electrode separated by a ~180 nm-wide gap. In principle, DA oxidation can be mediated both outer- and inner-sphere pathways to produce both adsorbed and non-adsorbed forms of DOQ. These pathways were unresolvable at slow scan rates (0.1 V s^{-1} in the top panel of Figure 1.14a), where diffusional voltammograms with a sigmoidal shape can be attributed to an outer- or inner-sphere pathway, or both [170], i.e. the Laviron–Amatore paradox. An inner-sphere pathway was manifested at faster scan rates (100 V s^{-1} in the top panel of Figure 1.14b) to yield surface waves at the generator electrode without a diffusional character. Accordingly, voltammetry at the single generator electrode cannot assess whether DA oxidation can be mediated through an outer-sphere pathway. By contrast, corrector responses were sigmoidal without an adsorption feature at all scan rates (the bottom panels of Figure 1.14a,b). At fast scan rates (e.g. 100 V s^{-1}), forward peaks at 0.45 V were due to capacitive coupling with the generator response and were not due to DOQ reduction at the collector electrode, because the forward peaks were observed even when the collector potential was too positive to reduce DOQ. Qualitatively, the sigmoidal shape of the collector response is attributed to the reduction of only DOQ that was generated through an outer-sphere pathway at the generator electrode, because the desorption of DOQ generated through an inner-sphere pathway at the generator electrode was too slow to yield a transient response at the collector electrode. More quantitatively, ~35% of DOQ should be desorbed from the generator electrode with a desorption rate constant of 22 s^{-1} [170] during the

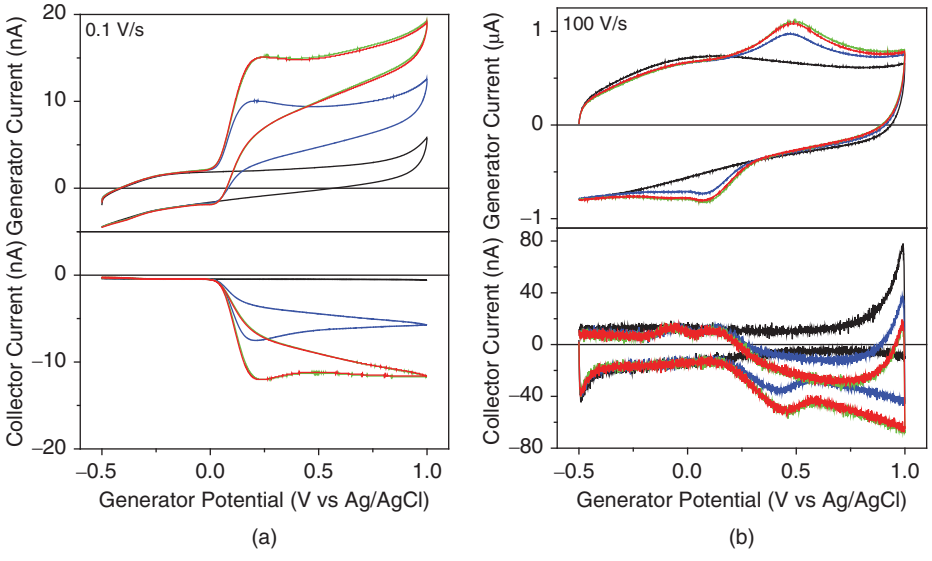

Figure 1.14 Generator and collector current responses of double-CF UMEs at (a) 0.1 and (b) 100 V s^{-1} in Tris buffer containing 0 (black), 50 (blue), and 100 (red and green for first and second cycles, respectively) μM DA. Collector potential at −0.3 V. Source: Reprinted with permission from Pathirathna et al. [148]. Copyright 2018 American Chemical Society.

potential cycle at 100 V s^{-1}. A larger amount of DOQ, however, was detected at the collector electrode at 100 V s^{-1}, where the charge under the voltammetric response of the collector electrode was larger than ~35% of the charge under the forward peak current based on DA oxidation at the generator electrode. This result supports that the collector response was at least partially attributed to the reduction of DOQ generated through an outer-sphere pathway at the generator electrode. More quantitative studies, however, are needed to unambiguously test the suggested mechanism and also to assess the contribution of self-exchange ET at the generator electrode to the collector response. Ideally, a generator electrode mediates all pathways at fast scan rates, not only to yield a current response dominated by inner-sphere and/or self-exchange pathway as demonstrated earlier by using single electrodes [22, 42], but also to minimize the desorption of a product generated through an inner pathway, thereby yielding a collector response dominated by the product generated through outer-sphere and/or self-exchange pathway at the generator electrode. A contribution of the second-order self-exchange pathway [29] may be assessed by varying DA concentrations in solution.

1.9 Summary and Perspectives

Adsorption-coupled ET is ubiquitous and important, but is also highly complicated and is not well understood despite many years of studies [171]. A voltammetric model based only on outer-sphere ET and surface adsorption of either reactant or product was quantitatively established ~50 years ago [126] even when adsorption and desorption steps were kinetically controlled [172]. Similarly, the coupling between outer- and inner-sphere ET through surface adsorption and self-exchange ET was recognized ~60 years ago [29] and has been quantitatively modeled since the 1980s [1, 42] to reveal the Laviron–Amatore paradox [21, 23]. A present convention, however, is to assign a redox couple to either outer- or inner-sphere one, which can cause controversies [43, 44]. Recent progress in nanoelectrochemical measurements [130, 148] as well as numerical simulation and data analysis [22, 111] may enable us to directly resolve outer- and inner-sphere ET and surface adsorption as elementary steps [24]. The importance of the interplay between outer- and inner-sphere pathways has been suggested for electrocatalysis [173, 174], which must involve inner-sphere pathways [4], but may also involve outer-sphere pathways [22], to facilitate the transfer of multiple electrons.

Acknowledgments

This work was supported by the National Science Foundation (CHE 1608703 and CHE 1904258) and the National Institutes of Health (R01 GM112656).

References

1 Laviron, E. (1982). Voltammetric methods for the study of adsorbed species. In: *Electroanalytical Chemistry*, vol. 12 (ed. A.J. Bard), 53. New York: Marcel Dekker.
2 Murray, R.W. (1984). Chemically modified electrodes. In: *Electroanalytical Chemistry*, vol. 13 (ed. A.J. Bard), 191. New York: Marcel Dekker.

3 Finklea, H.O. (1996). Electrochemistry of organized monolayers of thiols and related molecules on electrodes. In: *Electroanalytical Chemistry*, vol. 19 (eds. A.J. Bard and I. Rubinstein), 109. New York: Marcel Dekker.
4 Bard, A.J. (2010). *J. Am. Chem. Soc.* 132: 7559.
5 Switzer, J. (2015). Electrodeposition at the nanoscale. In: *Nanoelectrochemistry* (eds. M.V. Mirkin and S. Amemiya), 601. Boca Raton, FL: CRC Press.
6 Heinze, J., Frontana-Uribe, B.A., and Ludwigs, S. (2010). *Chem. Rev.* 110: 4724.
7 Martin, E.T., McGuire, C.M., Mubarak, M.S., and Peters, D.G. (2016). *Chem. Rev.* 116: 15198.
8 Rodeberg, N.T., Sandberg, S.G., Johnson, J.A. et al. (2017). *ACS Chem. Neurosci.* 8: 221.
9 McCreery, R.L. (1991). Carbon electrodes: structural effects on electron transfer kinetics. In: *Electroanalytical Chemistry*, vol. 17 (ed. A.J. Bard), 221. New York: Marcel Dekker.
10 Pereira, L. (2008). *J. Liq. Chromatogr. Related Technol.* 31: 1687.
11 McCreery, R.L. (2008). *Chem. Rev.* 108: 2646.
12 Dicks, A.L. (2006). *J. Power Sources* 156: 128.
13 Chakrabarti, M.H., Brandon, N.P., Hajimolana, S.A. et al. (2014). *J. Power Sources* 253: 150.
14 Brennan, L.J., Byrne, M.T., Bari, M., and Gun'ko, Y.K. (2011). *Adv. Energy Mater.* 1: 472.
15 Pandolfo, A.G. and Hollenkamp, A.F. (2006). *J. Power Sources* 157: 11.
16 McCreery, R.L. and Cline, K.K. (1996). Carbon electrodes. In: *Laboratory Techniques in Electroanalytical Chemistry* (eds. P.T. Kissinger and W.R. Heineman), 293. New York: Marcel Dekker.
17 Li, Z., Wang, Y., Kozbial, A. et al. (2013). *Nat. Mater.* 12: 925.
18 McCreery, R.L. (1999). Electrochemical properties of carbon surfaces. In: *Interfacial Electrochemistry: Theory, Experiment, and Applications* (ed. A. Wieckowski), 631. New York: Marcel Dekker.
19 Swain, G.M. (2004). Electrically conducting diamond thin films: advanced electrode materials for electrochemical technologies. In: *Electroanalytical Chemistry*, vol. 22 (eds. A.J. Bard and I. Rubinstein), 181. New York: Marcel Dekker.
20 McCreery, R.L. and McDermott, M.T. (2012). *Anal. Chem.* 84: 2602.
21 Klymenko, O.V., Svir, I., and Amatore, C. (2013). *J. Electroanal. Chem.* 688: 320.
22 Klymenko, O.V., Buriez, O., Labbe, E. et al. (2014). *ChemElectroChem* 1: 227.
23 Laviron, E. and Roullier, L. (1998). *J. Electroanal. Chem.* 443: 195.
24 Klymenko, O.V., Svir, I., and Amatore, C. (2014). *Mol. Phys.* 112: 1273.
25 Amemiya, S. (2015). Nanoscale scanning electrochemical microscopy. In: *Electroanalytical Chemistry*, vol. 26 (eds. A.J. Bard and C.G. Zoski), 1. Boca Raton, FL: CRC Press.
26 Kai, T., Zoski, C.G., and Bard, A. (2018). *J. Chem. Commun.* 54: 1934.
27 Amemiya, S., Chen, R., Nioradze, N., and Kim, J. (2016). *Acc. Chem. Res.* 49: 2007.
28 Bard, A.J. and Faulkner, L.R. (2001). *Electrochemical Methods: Fundamentals and Applications*, 2e, 13. New York: Wiley.
29 Anson, F.C. (1961). *Anal. Chem.* 33: 1498.
30 Anson, F.C. (1961). *Anal. Chem.* 33: 939.
31 Christensen, C.R. and Anson, F.C. (1963). *Anal. Chem.* 35: 205.
32 McDuffie, B., Anderson, L.B., and Reilley, C.N. (1966). *Anal. Chem.* 38: 883.

33 White, H.S. and McKelvey, K. (2018). *Curr. Opin. Electrochem.* 7: 48.
34 Laitinen, H.A. and Randles, J.E.B. (1955). *Trans. Faraday Soc.* 51: 54.
35 Llopis, J., Fernández-Biarge, J., and Fernández, M.P. (1959). *Electrochim. Acta* 1: 130.
36 Senda, M. and Delahay, P. (1961). *J. Phys. Chem.* 65: 1580.
37 Brown, A.P. and Anson, F.C. (1978). *J. Electroanal. Chem. Interfacial Electrochem.* 92: 133.
38 Weaver, M.J. and Anson, F.C. (1975). *J. Am. Chem. Soc.* 97: 4403.
39 Weaver, M.J. and Anson, F.C. (1976). *Inorg. Chem.* 15: 1871.
40 Laviron, E. (1981). *J. Electroanal. Chem. Interfacial Electrochem.* 124: 19.
41 Laviron, E. (1982). *J. Electroanal. Chem. Interfacial Electrochem.* 140: 247.
42 Laviron, E. (1995). *J. Electroanal. Chem.* 382: 111.
43 McDermott, C.A., Kneten, K.R., and McCreery, R.L. (1993). *J. Electrochem. Soc.* 140: 2593.
44 Zhang, G.H., Tan, S.Y., Patel, A.N., and Unwin, P.R. (2016). *Phys. Chem. Chem. Phys.* 18: 32387.
45 Bard, A.J. and Faulkner, L.R. (2001). *Electrochemical Methods: Fundamentals and Applications*, 2e, 589. New York: Wiley.
46 Bard, A.J. and Faulkner, L.R. (2001). *Electrochemical Methods: Fundamentals and Applications*, 2e, 31. New York: Wiley.
47 Bard, A.J. and Faulkner, L.R. (2001). *Electrochemical Methods: Fundamentals and Applications*, 2e, 590. New York: Wiley.
48 Bard, A.J. and Faulkner, L.R. (2001). *Electrochemical Methods: Fundamentals and Applications*, 2e, 52. New York: Wiley.
49 Gieseking, R.L.M., Ratner, M.A., and Schatz, G.C. (2018). *J. Phys. Chem. A* 122: 6809.
50 Siriwardhane, T., Ou, Y., Pathirathna, P., and Hashemi, P. (2018). *Anal. Chem.* 90: 11917.
51 Nioradze, N., Chen, R., Kurapati, N. et al. (2015). *Anal. Chem.* 87: 4836.
52 Chen, R., Nioradze, N., Santhosh, P. et al. (2015). *Angew. Chem. Int. Ed.* 54: 15134.
53 Velický, M., Bradley, D.F., Cooper, A.J. et al. (2014). *ACS Nano* 8: 10089.
54 Velický, M., Bissett, M.A., Toth, P.S. et al. (2015). *Phys. Chem. Chem. Phys.* 17: 17844.
55 Cuharuc, A.S., Zhang, G., and Unwin, P.R. (2016). *Phys. Chem. Chem. Phys.* 18: 4966.
56 Climent, V. and Feliu, J. (2011). *J. Solid State Electrochem.* 15: 1297.
57 Clavilier, J., Faure, R., Guinet, G., and Durand, R. (1980). *J. Electroanal. Chem.* 107: 205.
58 Swain, G.M. (2007). Solid electrode materials: pretreatment and activation. In: *Handbook of Electrochemistry* (ed. C.G.), 111. New York: Elsevier.
59 Kozbial, A., Li, Z., Conaway, C. et al. (2014). *Langmuir* 30: 8598.
60 Kozbial, A., Li, Z., Sun, J. et al. (2014). *Carbon* 74: 218.
61 Li, Z., Kozbial, A., Nioradze, N. et al. (2016). *ACS Nano* 10: 349.
62 Conway, B.E., Angerstein-Kozlowska, H., Sharp, W.B.A., and Criddle, E.E. (1973). *Anal. Chem.* 45: 1331.
63 Maekoya, C. and Okajima, Y. (1988). *Nippon Kagaku Kaishi* 6: 911.

64 Regnault, C., Kano, I., Darbouret, D., and Mabic, S. (2004). *J. Chromatogr. A* 1030: 289.
65 Scherson, D.A. and Tolmachev, Y.V. (2010). *Electrochem. Solid-State Lett.* 13: F1.
66 Wastl, D.S., Speck, F., Wutscher, E. et al. (2013). *ACS Nano* 7: 10032.
67 McDermott, M.T., Kneten, K., and McCreery, R.L. (1992). *J. Phys. Chem.* 96: 3124.
68 Patel, A.N., Collignon, M.G., O'Connell, M.A. et al. (2012). *J. Am. Chem. Soc.* 134: 20117.
69 Zhang, G., Cuharuc, A.S., Guell, A.G., and Unwin, P.R. (2015). *Phys. Chem. Chem. Phys.* 17: 11827.
70 Frederix, P., Bosshart, P.D., Akiyama, T. et al. (2008). *Nanotechnology* 19: 384004.
71 Wain, A.J., Pollard, A.J., and Richter, C. (2014). *Anal. Chem.* 86: 5143.
72 Lai, S.C.S., Patel, A.N., McKelvey, K., and Unwin, P.R. (2012). *Angew. Chem. Int. Ed.* 51: 5405.
73 Morteza Najarian, A., Chen, R., Balla, R.J. et al. (2017). *Anal. Chem.* 89: 13532.
74 Blackstock, J.J., Rostami, A.A., Nowak, A.M. et al. (2004). *Anal. Chem.* 76: 2544.
75 Yan, H., Bergren, A.J., and McCreery, R.L. (2011). *J. Am. Chem. Soc.* 133: 19168.
76 Morteza Najarian, A., Szeto, B., Tefashe, U.M., and McCreery, R.L. (2016). *ACS Nano* 10: 8918.
77 Tefashe, U.M., Nguyen, Q.V., Lafolet, F. et al. (2017). *J. Am. Chem. Soc.* 139: 7436.
78 Morteza Najarian, A. and McCreery, R.L. (2017). *ACS Nano* 11: 3542.
79 Mattson, J.S. and Smith, C.A. (1975). *Anal. Chem.* 47: 1122.
80 DeAngelis, T.P., Hurst, R.W., Yacynych, A.M. et al. (1977). *Anal. Chem.* 49: 1395.
81 Bardi, U., Magnanelli, S., and Rovida, G. (1986). *Surf. Sci.* 165: L7.
82 Chen, S. and Kucernak, A. (2004). *J. Phys. Chem. B* 108: 3262.
83 Nioradze, N., Kim, J., and Amemiya, S. (2011). *Anal. Chem.* 83: 828.
84 Nioradze, N., Chen, R., Kim, J. et al. (2013). *Anal. Chem.* 85: 6198.
85 Zoski, C.G., Aguilar, J.C., and Bard, A. (2003). *J. Anal. Chem.* 75: 2959.
86 Rodgers, P.J., Amemiya, S., Wang, Y., and Mirkin, M.V. (2010). *Anal. Chem.* 82: 84.
87 Wang, Y., Velmurugan, J., Mirkin, M.V. et al. (2010). *Anal. Chem.* 82: 77.
88 Bard, A.J., Mirkin, M.V., Unwin, P.R., and Wipf, D.O. (1992). *J. Phys. Chem.* 96: 1861.
89 Tan, S.Y., Zhang, J., Bond, A.M. et al. (2017). *Anal. Chem.* 89: 7273.
90 Kim, J., Renault, C., Nioradze, N. et al. (2016). *J. Am. Chem. Soc.* 138: 8560.
91 Chen, R., Hu, K., Yu, Y. et al. (2016). *J. Electrochem. Soc.* 163: H3032.
92 Kim, J., Renault, C., Nioradze, N. et al. (2016). *J. Anal. Chem.* 88: 10284.
93 Kim, J., Shen, M., Nioradze, N., and Amemiya, S. (2012). *Anal. Chem.* 84: 3489.
94 Sun, P. and Mirkin, M.V. (2006). *Anal. Chem.* 78: 6526.
95 Velmurugan, J., Sun, P., and Mirkin, M.V. (2008). *J. Phys. Chem. C* 113: 459.
96 Yu, Y., Sun, T., and Mirkin, M.V. (2016). *Anal. Chem.* 88: 11758.
97 Penner, R.M., Heben, M.J., Longin, T.L., and Lewis, N.S. (1990). *Science* 250: 1118.
98 Oldham, K.B. (1992). *Anal. Chem.* 64: 646.
99 Shao, Y., Mirkin, M.V., Fish, G. et al. (1997). *Anal. Chem.* 69: 1627.
100 Porat, Z., Crooker, J.C., Zhang, Y. et al. (1997). *Anal. Chem.* 69: 5073.
101 Katemann, N.B. and Schuhmann, W. (2002). *Electroanalysis* 14: 22.
102 Actis, P., Tokar, S., Clausmeyer, J. et al. (2014). *ACS Nano* 8: 875.
103 Clausmeyer, J. and Schuhmann, W. (2016). *TrAC, Trends Anal. Chem.* 79: 46.
104 Chen, R., Balla, R.J., Li, Z.T. et al. (2016). *Anal. Chem.* 88: 8323.

105 Snowden, M.E., Guell, A.G., Lai, S.C.S. et al. (2012). *Anal. Chem.* 84: 2483.
106 Güell, A.G., Ebejer, N., Snowden, M.E. et al. (2012). *Proc. Natl. Acad. Sci. U. S. A.* 109: 11487.
107 Güell, A.G., Meadows, K.E., Dudin, P.V. et al. (2014). *Nano Lett.* 14: 220.
108 Marcus, R.A. (1965). *J. Chem. Phys.* 43: 679.
109 Feldberg, S.W. and Sutin, N. (2006). *Chem. Phys.* 324: 216.
110 Tan, S.-Y., Zhang, J., Bond, A.M. et al. (2016). *Anal. Chem.* 88: 3272.
111 Kurapati, N., Pathirathna, P., Chen, R., and Amemiya, S. (2018). *Anal. Chem.* 90: 13632.
112 Amemiya, S. (2017). *Anal. Chem.* 89: 7269.
113 Tsujioka, N., Imakura, S., Nishi, N., and Kakiuchi, T. (2006). *Anal. Sci.* 22: 667.
114 Rodgers, P.J. and Amemiya, S. (2007). *Anal. Chem.* 79: 9276.
115 Li, W., Tan, C., Lowe, M.A. et al. (2011). *ACS Nano* 5: 2264.
116 Ritzert, N.L., Rodriguez-Lopez, J., Tan, C., and Abruña, H.D. (2013). *Langmuir* 29: 1683.
117 Zhong, J.-H., Zhang, J., Jin, X. et al. (2014). *J. Am. Chem. Soc.* 136: 16609.
118 Güell, A.G., Ebejer, N., Snowden, M.E. et al. (2012). *J. Am. Chem. Soc.* 134: 7258.
119 Li, X.S., Cai, W.W., An, J.H. et al. (2009). *Science* 324: 1312.
120 Lin, Y.C., Lu, C.C., Yeh, C.H. et al. (2012). *Nano Lett.* 12: 414.
121 Lisi, N., Dikonimos, T., Buonocore, F. et al. (2017). *Sci. Rep.* 7: 9927.
122 Ge, X., Zhang, Y., Chen, L. et al. (2018). *Carbon* 139: 989.
123 Masel, R.I. (1996). *Principles of Adsorption and Reaction on Solid Surfaces*. New York: Wiley.
124 Bard, A.J. and Faulkner, L.R. (2001). *Electrochemical Methods: Fundamentals and Applications*, 2e, 567. New York: Wiley.
125 Bradbury, C.R., Kuster, L., and Fermin, D.J. (2010). *J. Electroanal. Chem.* 646: 114.
126 Wopschall, R.H. and Shain, I. (1967). *Anal. Chem.* 39: 1514.
127 Costentin, C., Dridi, H., and Saveant, J.M. (2015). *J. Am. Chem. Soc.* 137: 13535.
128 Leverenz, A. and Speiser, B. (1991). *J. Electroanal. Chem. Interfacial Electrochem.* 318: 69.
129 Schulz, C. and Speiser, B. (1993). *J. Electroanal. Chem.* 354: 255.
130 Chen, R., Najarian, A.M., Kurapati, N. et al. (2018). *Anal. Chem.* 90: 11115.
131 Amatore, C., Savéant, J.M., and Tessier, D. (1983). *J. Electroanal. Chem.* 147: 39.
132 Sliusarenko, O., Oleinick, A., Svir, I., and Amatore, C. (2015). *ChemElectroChem* 2: 1279.
133 Sliusarenko, O., Oleinick, A., Svir, I., and Amatore, C. (2015). *Electroanalysis* 27: 980.
134 Laviron, E. (1974). *J. Electroanal. Chem. Interfacial Electrochem.* 52: 355.
135 Miao, W., Ding, Z., and Bard, A.J. (2002). *J. Phys. Chem. B* 106: 1392.
136 Bhat, M.A., Nioradze, N., Kim, J. et al. (2017). *J. Am. Chem. Soc.* 139: 15891.
137 Cornell, R.M. and Schwertmann, U. (1996). *The Iron Oxides*. Weinheim, Germany: VCH.
138 Sorenson, T.A., Morton, S.A., Waddill, G.D., and Switzer, J.A. (2002). *J. Am. Chem. Soc.* 124: 7604.
139 Switzer, J.A., Gudavarthy, R.V., Kulp, E.A. et al. (2010). *J. Am. Chem. Soc.* 132: 1258.
140 Gudavarthy, R.V., Miller, A.S., Bohannan, E.W. et al. (2011). *Electrochim. Acta* 56: 10550.

141 Vago, E.R. and Calvo, E.J. (1992). *J. Electroanal. Chem.* 339: 41.
142 Wu, Z.-S., Yang, S., Sun, Y. et al. (2012). *J. Am. Chem. Soc.* 134: 9082.
143 Zhang, X., Wang, X., Le, L. et al. (2015). *J. Mater. Chem. A* 3: 19273.
144 Zhao, C., Ma, Y., Shen, C., and Han, W. (2016). *J. Nanosci. Nanotechnol.* 16: 950.
145 Kulp, E.A., Kothari, H.M., Limmer, S.J. et al. (2009). *Chem. Mater.* 21: 5022.
146 Helu, M.A.B., Bonazza, H.L., and Fernandez, J.L. (2016). *J. Electroanal. Chem.* 775: 64.
147 Helu, M.A.B. and Fernandez, J.L. (2017). *J. Electroanal. Chem.* 784: 33.
148 Pathirathna, P., Balla, R.J., and Amemiya, S. (2018). *Anal. Chem.* 90: 11746.
149 Hupp, J.T., Liu, H.Y., Farmer, J.K. et al. (1984). *J. Electroanal. Chem. Interfacial Electrochem.* 168: 313.
150 Kim, J. and Bard, A.J. (2016). *J. Am. Chem. Soc.* 138: 975.
151 Bano, K., Zhang, J., Bond, A.M. et al. (2015). *J. Phys. Chem. C* 119: 12464.
152 Smalley, J.F., Finklea, H.O., Chidsey, C.E.D. et al. (2003). *J. Am. Chem. Soc.* 125: 2004.
153 Smalley, J.F., Geng, L., Chen, A. et al. (2003). *J. Electroanal. Chem.* 549: 13.
154 Aoki, K.J., Chen, J., and Tang, P.J. (2018). *Phys. Chem. C* 122: 16727.
155 Cabaniss, G.E., Diamantis, A.A., Murphy, W.R. et al. (1985). *J. Am. Chem. Soc.* 107: 1845.
156 Mohilner, D.M. (1969). *J. Phys. Chem.* 73: 2652.
157 He, Z.-D., Chen, Y.-X., Santos, E., and Schmickler, W. (2018). *Angew. Chem. Int. Ed.* 57: 7948.
158 Ghosh, S., Horvath, S., Soudackov, A.V., and Hammes-Schiffer, S. (2014). *J. Chem. Theory Comput.* 10: 2091.
159 Gerischer, H. (1976). Electron transfer and electrocatalysis. In: *Electrocatalysis on Non-metal Surfaces* (ed. A.D. Franklin), 1. Gaithersburg, MD: National Bureau of Standards.
160 DuVall, S.H. and McCreery, R.L. (1999). *Anal. Chem.* 71: 4594.
161 Bard, A.J. and Faulkner, L.R. (2001). *Electrochemical Methods: Fundamentals and Applications*, 2e, 566. New York: Wiley.
162 Bard, A.J. and Faulkner, L.R. (2001). *Electrochemical Methods: Fundamentals and Applications*, 2e, 60. New York: Wiley.
163 DuVall, S.H. and McCreery, R.L. (2000). *J. Am. Chem. Soc.* 122: 6759.
164 Laviron, E. (1979). *J. Electroanal. Chem.* 101: 19.
165 Laviron, E. and Roullier, L. (1983). *J. Electroanal. Chem.* 157: 7.
166 Laviron, E., Meunierprest, R., Vallat, A. et al. (1992). *J. Electroanal. Chem.* 341: 227.
167 Lacasse, R., Meunierprest, R., Laviron, E., and Vallat, A. (1993). *J. Electroanal. Chem.* 359: 223.
168 Laviron, E., Meunierprest, R., and Lacasse, R.J. (1994). *J. Electroanal. Chem.* 375: 263.
169 Pathirathna, P., Balla, R.J., and Amemiya, S. (2018). *J. Electrochem. Soc.* 165: G3026.
170 Bath, B.D., Michael, D.J., Trafton, B.J. et al. (2000). *Anal. Chem.* 72: 5994.
171 Heyrovsky, J. and Kuta, J. (1965). *Principles of Polarography*, 287. New York: Academic Press.
172 Hulbert, M.H. and Shain, I. (1970). *Anal. Chem.* 42: 162.
173 Ramaswamy, N. and Mukerjee, S.J. (2011). *Phys. Chem. C* 115: 18015.
174 Bonnefont, A., Ryabova, A.S., Schott, T. et al. (2019). *Curr. Opin. Electrochem.* 14: 23.